

GTC spectra of $z \approx 2.3$ quasars: comparison with local luminosity analogs^{★,★★}

Jack W. Sulentic¹, Paola Marziani², Ascensión del Olmo¹, Deborah Dultzin³, Jaime Perea¹, and C. Alenka Negrete⁴

¹ Instituto de Astrofísica de Andalucía, IAA-CSIC, Glorieta de la Astronomía s/n, 18008 Granada, Spain
e-mail: [sulentic;chony;jaime]@iaa.es

² INAF, Osservatorio Astronomico di Padova, vicolo dell' Osservatorio 5, 35122 Padova, Italy
e-mail: paola.marziani@oapd.inaf.it

³ Instituto de Astronomía, Universidad Nacional Autónoma de México, 04510 Mexico D.F., Mexico
e-mail: deborah@astro.unam.mx

⁴ Instituto Nacional de Astrofísica, Óptica y Electrónica, Tonantzintla, Puebla, Mexico
e-mail: cnegrete@inaoep.mx

Received 10 April 2014 / Accepted 16 June 2014

ABSTRACT

Context. The advent of 8–10 m class telescopes for the first time makes it possible to compare in detail quasars with similar luminosity and very different redshifts.

Aims. We conducted a search for z -dependent gradients in line-emission diagnostics and derived physical properties by comparing, in a narrow bolometric luminosity range ($\log L \sim 46.1 \pm 0.4$ [erg s⁻¹]), some of the most luminous local $z < 0.6$ quasars with some of the lowest luminosity sources yet found at redshift $z = 2.1$ – 2.5 .

Methods. Moderate signal-to-noise ratio spectra for 22 high-redshift sources were obtained with the 10.4 m Gran Telescopio Canarias (GTC), for which the HST (largely the Faint Object Spectrograph) archive provides a low-redshift control sample. We compared the spectra in the context of the 4D Eigenvector 1 formalism, meaning that we divided both source samples into highly accreting population A and population B sources accreting at a lower rate.

Results. CIV λ 1549, the strongest and most reliable diagnostic line, shows very similar properties at both redshifts, which confirms the CIV λ 1549 profile differences at high redshift between populations A and B, which are well established in local quasars. The CIV λ 1549 blueshift that appears quasi-ubiquitous in higher L sources is found in only half (population A) of the quasars observed in the two samples. A CIV λ 1549 evolutionary Baldwin effect is certainly disfavored. We find evidence for lower metallicity in the GTC sample that may point toward a gradient with z . No evidence for a gradient in M_{BH} or L/L_{Edd} is found.

Conclusions. Spectroscopic differences established at low z are also present in much higher redshift quasars. Our results on the CIV λ 1549 blueshift suggest that it depends both on source luminosity and L/L_{Edd} . Given that our samples involve sources with very similar luminosity, the evidence for a systematic metallicity decrease, if real, points toward an evolutionary effect. Our samples are not large enough to effectively constrain possible changes of M_{BH} or L/L_{Edd} with redshift. The two samples appear representative of a slowly evolving quasar population that is most likely present at all redshifts.

Key words. quasars: emission lines – quasars: supermassive black holes – ISM: abundances – line: profiles – cosmology: observations

1. Introduction

It has been known for decades that quasars show evolution with redshift (Schmidt 1968; Schmidt & Green 1983). The brightest quasars at redshifts $z \gg 1.0$ are much more luminous than any local quasars (often called Seyfert 1s if they show a host galaxy). Locally ($z \lesssim 0.5$), we find quasars with absolute magnitudes in the range $M_B = -23$ to -25 (we ignore here AGN below -23 , which was a kind of historical boundary between type 1 quasars and Seyfert 1 galaxies). At redshift $z \approx 2.3$ (the quasar number density peaks near this redshift: Schmidt et al. 1995; Boyle et al. 2000) we find sources in the range $M_B = -25$ to -29 , while sources in this luminosity range are locally almost nonexistent. At redshift $z \approx 4$ we observe $M_B = -27$ to -30 superluminous quasars that are 2 dex more luminous than any local sources.

* Full Figs. 4 and 5 and Appendix A are available in electronic form at <http://www.aanda.org>

** Reduced spectra as FITS files are only available at the CDS via anonymous ftp to cdsarc.u-strasbg.fr (130.79.128.5) or via <http://cdsarc.u-strasbg.fr/viz-bin/qcat?J/A+A/570/A96>

We are forced to conclude that the most luminous quasars show strong evolution in their space density. In fact, they no longer exist. Does this mean that all quasars show evolution, or is it purely luminosity driven? Figure 1 illustrates the observational situation by plotting the distribution of a representative SDSS quasar subsample (Schneider et al. 2010) in the $z - B$ absolute magnitude plane. Note that only sources listed as quasars in the Schneider et al. (2010) catalogs are shown, so that a large population of local active galactic nuclei (AGN; Koehler et al. 1997) and AGN with the narrowest broad lines ($FWHM < 1000$ km s⁻¹; Zhou et al. 2006) are not shown in the lower part of the plot. The low- z yellow box identifies a range of absolute magnitudes where quasars are rare in the local Universe (they would be easily detected, but they do not exist in large numbers) and belong to the high-luminosity tail of the optical luminosity function (Cheng et al. 1985; Grazian et al. 2000; Richards et al. 2005). If analogs to local quasars exist at all redshifts, the lower right quadrant of the plot will be well populated when they are found. They would be generally fainter than $m_B \approx 22$ and until very recently were not easy to find; however,

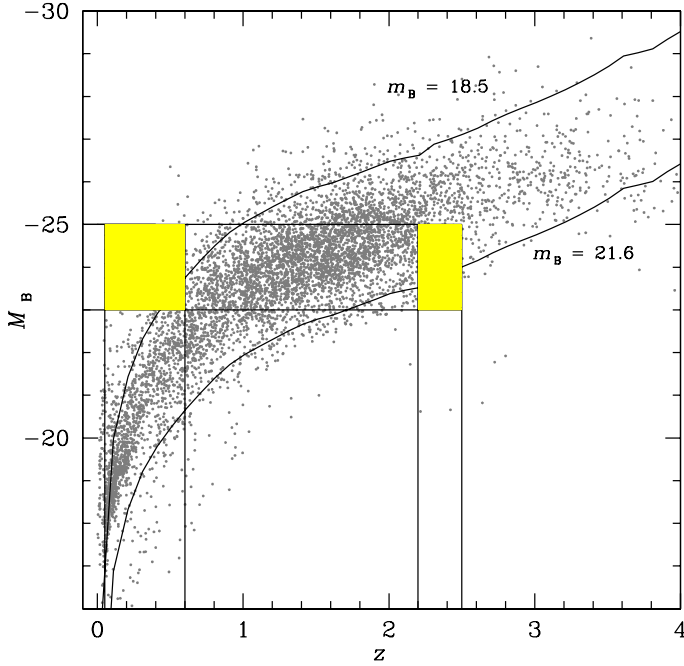


Fig. 1. Absolute magnitude of quasars vs. redshift for the SDSS-based catalog of Schneider et al. (2010). Curves are computed for two limiting (K-corrected) apparent magnitudes $m_B = 18.5$ and $m_B = 21.6$. The shaded boxes identify the loci in the $z - M_B$ planes of two volume-limited samples within the same luminosity limits: one between $2.2 \leq z \leq 2.5$ as for the GTC sample of this paper, and a control sample at $0.05 \leq z \leq 0.6$.

that situation is changing rapidly thanks to SDSS-III/BOSS (Ahn et al. 2014).

Historical attempts to compare quasars with similar luminosity at significantly different redshifts were few and difficult. We have more often compared the brightest quasars at different redshifts because it has been almost impossible to obtain good spectra for fainter sources (luminosity analogs of low- z sources) using 2–4 m class telescopes. This means that we are usually comparing quasars in very different optical luminosity ranges. This limitation is quite relevant if optical luminosity plays an important role in quasar evolution and obscures other physical drivers. We are unable to search effectively for signatures of luminosity-independent evolution (e.g. metallicity, BLR structure/geometry, M_{BH} , and accretion rate). Spectroscopy provides the most powerful clues about most of these things. Obtaining spectra for $z \geq 2.0$ – 2.5 luminosity analogs of nearby quasars involves spectroscopy of faint sources $m_B = 21$ – 23 . It is one thing to obtain spectra to confirm the existence of faint quasars and quite another to obtain spectra with a signal-to-noise ratio (S/N) and resolution that permit more detailed studies.

There is a growing consensus that the leading parameter that governs quasar diversity involves the Eddington ratio (e.g., Marziani et al. 2001; Baskin & Laor 2004; Dong et al. 2009; Brightman et al. 2013). Other factors most likely play important roles and have been discussed in recent reviews (e.g., Marziani et al. 2006; Marziani & Sulentic 2014a). We note that a key complication affecting the quasars is that our measurements are affected by line-of-sight orientation (Sulentic et al. 2003; Collin et al. 2006; Boroson 2011; Runnoe et al. 2013). Metallicity effects also significantly affect the observed spectra of quasars (e.g., Ferland et al. 1996; Shemmer et al. 2004; Netzer & Trakhtenbrot 2007).

One might ask whether high-redshift analogs of local low-luminosity quasars even exist. Perhaps all quasars were luminous “monsters” at high redshift, and we are witnessing a systematic downgrading of activity with increasing cosmic time. In this view, the youngest quasars at any epoch grow so fast that we observe very few in the process of rapid accretion. The currently favored view is that rapidly accreting monster quasars exist side by side with slower growing quasars (AGN), and that the latter exist at all redshifts (Trakhtenbrot et al. 2011). The monsters have gradually disappeared and are no longer seen below $z \approx 2.0$. The slower evolving quasar population is assumed to be plentiful, perhaps even more numerous than at low redshift. Is the peak in quasar density near $z \approx 2.3$ (e.g., Fan 2006) driven largely or totally by the luminous population that has ceased to exist? Do high-redshift analogs of local quasars show the same space density at all redshifts as well as the same emission line properties, black holes masses, and Eddington ratios? The few studies of low- L quasars at high z so far have focused on estimating the space density of these sources (Glikman et al. 2011; Ikeda et al. 2012). We focus instead on trying to answer some of the questions raised above. The fainter, assumed to be slower evolving, quasars of interest in this study are largely absent above $z \sim 1$ in Fig. 1 because they were not spectroscopically sampled by SDSS. Up to the present, they have more often been discovered in deep radio, X-ray, or optical pencil-beam surveys. At redshifts above $z \sim 1$, SDSS I/II surveyed quasars are largely brighter than $m_B \approx 20$ – 21 . If high-redshift analogs of low-luminosity/redshift quasars exist in abundance, are they spectroscopically different in any way? This question motivated our study.

One of the many technological changes that has taken place during the 50 years since the discovery of quasars involves the advent of 8–10 m class telescopes equipped with CCD imaging spectrographs. We are now entering the era when we can effectively compare quasars of very similar luminosity at very different redshifts. We report here on a pilot survey of $z \approx 2.1$ – 2.4 quasars with luminosities in the range $M_B = -23$ to -25 , which is the same range as low-luminosity quasars found at low z (down to the most luminous local Seyfert galaxies). Section 2 describes the survey, source sample, low- z control sample, and reduction procedures. Section 3 presents the high- z source spectra and emission line parameters derived from them. Section 3.2 presents a comparison of mean/median properties for the high and low- z samples. This is followed by comparison in the 4D Eigenvector (4DE1) context where we distinguish and compare Population A and B sources separately. Section 4 discusses implication of our findings in terms of quasar evolution, focusing on observational parameters, gas metallicity, black hole mass and Eddington ratio. Finally we present in Appendix A the analysis of a red quasar that showed up in our sample.

2. Spectroscopic samples and reductions

2.1. Sample selection strategy

The goal of the present study was to make a spectroscopic survey of quasars in the range $z = 2.1$ – 2.5 with luminosities similar to local sources. We required a high enough S/N to allow a detailed comparison with properties of a low-redshift control sample taken from the HST archive. This was a pencil-beam survey in the sense that the same spectral region ($Ly\alpha$ – $CIII\lambda 1909$) was sampled over a very narrow z , M_B range. The z range was chosen to be as high as possible to sample quasars at a cosmologically significant epoch. The M_B range involved luminosities

Table 1. Source identification and basic properties.

NED identification	m_V^a	z	δz	M_B^b	Discovery	Ref.	Alternative name	Notes
OH91 073	20.9	2.2630	0.0016	-24.4	grism/grens	1	NVSS J121848-110332, Q 1216-1046	NVSS 38.9 ± 1.6 mJy, RL serendipitous
OH91 119	20.9	2.2660	0.0005	-24.4	grism/grens	1	Q 1232-1059	
OH91 121	21.0	2.4065	0.0027	-23.8	grism/grens	1	Q 1232-1113	
B1.0334	21.6	2.2999	0.0012	-23.7	X-ray	2	SDSS J123742.52+621811.6	
Wee 87	20.8	2.2418	0.0022	-24.3	grism/grens	3	HB89 1257+357	
HB89 1340+277	21.4	2.1842	0.0023	-23.7	grism/grens	3	Q 1340+2744	
2QZ J134206.3-003702	20.3	2.2115	0.0028	-24.4	color (2dF)	4	SDSS J134206.34-003701.2	
F864:158	21.7	2.2297	0.0023	-23.4	color	5	SDSS J134423.95-002846.4	
2QZ J143400.0+002649	20.8	2.2054	0.0005	-24.3	color (2dF)	6		
FIRST J153150.4+242317	20.5	2.2841	0.0011	-24.7	IR	7	SDSS/F2M J153150.4+242317	Heavily obscured; RL serendipitous NVSS 138.9 ± 4.2 mJy
TXS 1529-230	21.4	2.2800	0.0020	-23.8	Radio	8	PMN J1532-2310	
CADIS 16h-1610	20.8	2.2717	0.0016	-24.2	color + FP?	9	SDSS J162359.21+554108.7	
CADIS 16h-1373	21.9	2.2780	0.0018	-23.2	color + FP?	9	SDSS J162421.29+554243.0	
Wee 155	21.0	1.5981	0.0049	-24.2	grism/grens	3	HB89 1634+332	$z \approx 2.37$ in catalogs
SDSS J164226.90+405034.3	20.4	2.3258	0.0005	-25.0	grism/grens	10	Q 1640+4056	
SPIT 17196+5922	20.7	2.2255	0.0015	-24.1	IR/ <i>Spitzer</i>	11	SDSS J171941.24+592242.1	
VCV96 1721.4+3401	20.9	2.3244	0.0055	-24.1	grism/grens	12	Q 1721+3400	
Wee 173	20.2	2.4144	0.0016	-25.3	grism/grens	3	HB89 1834+509	
Wee 174	20.6	2.2720	0.0008	-24.8	grism/grens	3	HB89 1835+509	
CXOMP J205620.5-043100	21.2	2.3299	0.0032	-23.6	X-ray	13	CXO J205620.5-043100	
VCV96 2240.7+0066	20.4	2.2579	0.0019	-24.5	grism/grens	12	Q 2240+0066	
CXOMP J234752.5+010306	20.5	2.4043	0.0014	-24.3	X-ray	13	SDSS J234752.55+010305.0	

Notes. ^(a) Indicative V magnitudes as reported by Véron-Cetty & Véron (2010). ^(b) Absolute B magnitude at $z = 0$ as tabulated by Véron-Cetty & Véron (2010).

References. 1) Osmer & Hewett (1991); 2) Brandt et al. (2001); 3) Weedman (1985); 4) Croom et al. (2001); 5) Boyle et al. (1991); 6) Croom et al. (2004); 7) Glikman et al. (2007); 8) Griffith et al. (1994); 9) Wolf et al. (1999); 10) Crampton et al. (1988); 11) Papovich et al. (2006); 12) Crampton et al. (1985); 13) Silverman et al. (2005).

as low as possible (just above the nominal Seyfert 1 – type 1 quasar boundary at $M_B = -23.0$). We would have preferred to go 1–2 magnitudes fainter, but the adopted range was dictated by available telescope time and instrumentation. This translates into sources in the apparent magnitude range $m_B \sim 20.0$ – 22.0 , which corresponds to $M_B \approx -23$ to -25 (and bolometric luminosity $\log L \sim 45.7$ – 46.5).

Steps to find low luminosity quasars at $z \approx 2.5$ involved a search for faint previously identified quasars in the Véron-Cetty & Véron catalog (e.g., Véron-Cetty & Véron 2010), since we did not carry out a new quasar survey. Many of our adopted targets are SDSS sources, but lacked spectroscopic follow-up in either SDSS-I/II or SDSS-III/BOSS at the time of our survey. Sources were selected in ranges of narrow redshift ($2.3 \lesssim z \lesssim 2.5$) and absolute magnitude ($-25 \lesssim M_B \lesssim -23$). The high- and low- z regions of interest are marked in Fig. 1. More than 2700 candidate sources are found in the 13th edition of Véron-Cetty & Véron (2010). Clearly, the number of low- and intermediate-luminosity quasars at high z is increasing rapidly. Targets were selected randomly and are listed in Table 1, which presents quasar identification, apparent magnitude, redshift $\pm 1\sigma$ uncertainty (see Sect. 2.3), absolute B magnitude from Véron-Cetty & Véron (2010), discovery technique or detection band, a reference to the discovery paper, an alternate name, and some additional information notably on radio flux for radio-detected sources. As expected, many chosen sources have names reflecting discovery in X-ray surveys or deep optical searches (Table 1, Cols. 7–8). The flux limits associated with optical surveys cause an Eddington ratio bias, as shown in Fig. 2. Figure 2 gives a graphical representation for the case of a typical ($10^8 M_\odot$) and a large black hole mass ($10^{9.5} M_\odot$). Bands of different colors

identify sources radiating in different Eddington ranges. Sources radiating close to or somewhat below the Eddington limit are indicated as NLSy1-like quasars (population A in 4DE1 parlance, Sulentic et al. 2000b; Netzer 2013 and Sect. 4). Below $L/L_{\text{Edd}} \approx 0.2$ we find no change in observational properties (population B; Sulentic et al. 2008, 2011), while below $L/L_{\text{Edd}} \approx 0.01$ accretion processes may become unstable and the quasar state may be transient. The flux limit associated with a survey introduces a bias in the discovery of quasars: in the example of Fig. 2 all quasars at $z \lesssim 0.3$ with $M_{\text{BH}} = 10^8 M_\odot$ can be detected, while at $z \approx 2.3$ only quasars radiating close to the Eddington limit will be detected within a limiting magnitude $m_B \approx 21.5$. Only quasars with the largest masses will be detected at $z \approx 2.3$. This mass-dependent loss of low Eddington ratio sources will be a source of bias at high z .

2.2. Observations and data reduction

By using the 10 m GTC equipped with the faint-object spectrograph OSIRIS (Optical System for Imaging and low-Intermediate-Resolution Integrated Spectroscopy), it is possible to obtain $S/N \approx 20$ spectra of quasars in the $m_B \approx 21$ – 22 mag range with exposures of about 40 min in good seeing. Under less than optimal conditions we will obtain spectra with $S/N \approx 7$ – 12 . Within the observed wavelength range we obtained several lines (from Ly α to CIII] $\lambda 1909$) from which diagnostics intensity ratios can be computed. The GTC spectra are similar to or better than the HST archival UV spectra for low-redshift analogs (Bachev et al. 2004; Sulentic et al. 2007). Figure 3 shows a montage of the deredshifted GTC spectra obtained for 22 quasars. One source (Wee 155) turned out to have an

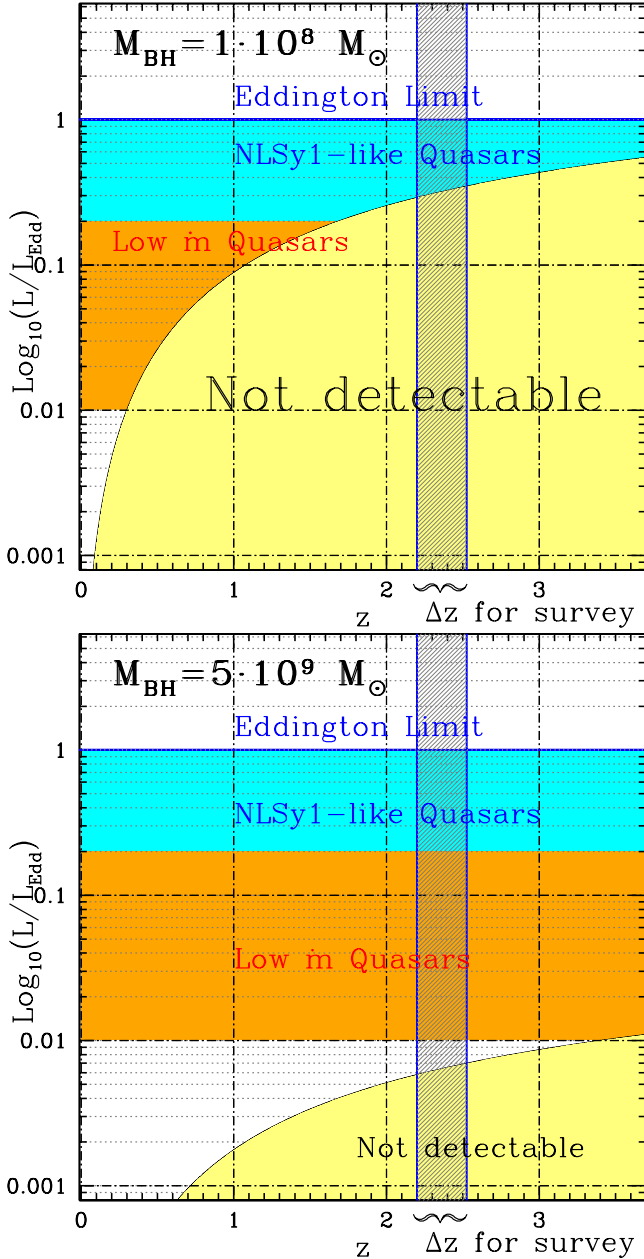


Fig. 2. Eddington ratio as a function of redshift, with the area of undetectable sources below a limiting magnitude $m_B \approx 21.5$ in yellow. The redshift range of the quasar survey is identified by the dashed strip. See text for further details.

incorrect redshift ($z \approx 1.59$) derived from the low S/N discovery spectrum. An additional source is obviously a heavily reddened (radio-loud if no correction for extinction is applied) quasar FIRST J15318+2423 (discussed in Appendix A). The remaining 20 sources represent our working sample of unreddened low-luminosity quasars (two are radio loud). Spectra show an S/N near 10–20, covering $\text{Ly}\alpha - \text{CIII}]1909$ in the rest frame. They can be effectively compared with low- z UV spectra from the HST archive that were previously studied in the 4DE1 context (Bachev et al. 2004; Sulentic et al. 2007). Our high- z sample clusters near $\log L_{\text{bol}} \sim 46.0$ with redshift range from $z = 2.21$ – 2.40 .

Long-slit spectroscopic observations of the selected quasars were carried out with OSIRIS, which is located at the Nasmyth-B focus of the 10.4m GTC telescope of the Observatorio del

Roque de los Muchachos (La Palma, Spain). The observations were obtained in service mode in two approved observing programs during 2011 and 2013. In the first run 15 QSOs were observed, while 7 more were obtained during the spring 2013 run. The R1000B grism was used for all observations with 2×2 binning, yielding a wavelength range of 3650–7750 Å with a reciprocal dispersion of about 2.1 Å/pixel ($R = \lambda/\delta\lambda \approx 1000$). This coverage corresponds to the wavelength region of interest for our study from $\text{Ly}\alpha$ to $\text{CIII}]1909$ and includes $\text{NV}\lambda 1240$, $\text{SiIV}\lambda 1397$ and $\text{OIV}]\lambda 1402$, $\text{CIV}\lambda 1549$, $\text{AlIII}\lambda 1860$, or $\text{SiIII}]\lambda 1892$ emission lines. The slit was oriented at parallactic angle to minimize effects of atmospheric differential refraction in the spectra. The columns in Table 2 list the observation log in this order: QSO ID, date of observation, total exposure time in seconds, the number of split exposures, the S/N measured in the combined spectrum for each object (at 1450 Å; blueward of the $\text{CIV}\lambda 1549$ line), the slit width in arcsec, and the seeing measured by fitting several stars in the acquisition image of each quasar.

Data reduction was carried out in a standard way using the IRAF package. The task CCDPROC was used to trim the spectra and make the overscan correction. Bias subtraction was performed nightly by subtracting a median zero-level bias image constructed by combining all bias frames provided by the telescope team. In addition, each spectrum was flat-field corrected with the normalized flat-field obtained after median combination of the flats obtained with the same instrumental setup. Two-dimensional wavelength calibration was obtained using the combination of HgAr and Ne lamp exposures and IRAF routines IDENTIFY, REIDENTIFY, FITCOORDS, and TRANSFORM. We checked the wavelength calibration for all the individual exposures of each objects before final combination. The APALL task was used for object extraction and background subtraction. Instrumental response and flux calibration were obtained from spectrophotometric standard star exposures with the same instrumental configuration, which were provided for each night our sources were observed (Ross 640, Feige 34, GD 24, GRW+70.8247 and Feige 92 [for the first run]; Feige92, Ross 640, G157-32 and GD 140 [for the second run]).

2.3. Data analysis

Spectra were reduced to rest-frame wavelength and specific flux scale. An unbiased estimate of the redshift (i.e., source rest frame) is not trivial because the GTC spectra only cover the UV domain where narrow low-ionization lines (LILs), usually the most reliable rest-frame indicators (Eracleous & Halpern 2003; Hu et al. 2008), are not available. We therefore only estimated redshifts from low-ionization $\text{OI}\lambda 1304$, $\text{SiII}\lambda 1264$, $\text{CII}\lambda 1334$ features as well as $\text{CIII}]\lambda 1909$, including $\text{CIV}\lambda 1549$ and other high-ionization lines if they showed values consistent with the LILs. Uncertainties are reported in Table 1 with the rest frame estimated to be accurate to $\pm 200 \text{ km s}^{-1}$ for most sources ($\pm 300 \text{ km s}^{-1}$ for three sources). The LIL features were not measured in one source ([VCV96] 1721.4+3401), which means that the redshift is based on $\text{CIV}\lambda 1549$, $\text{Ly}\alpha$, and $\text{SiIII}]\lambda 1892$. The first two lines yield a significantly lower value than $\text{SiIII}]\lambda 1892$, leading to an estimated uncertainty of $\pm 500 \text{ km s}^{-1}$.

One of the first steps after data reduction was an attempt to separate sources into populations A and B following the 4DE1 formalism. The optical and UV (as well as X-ray) criteria are summarized in Sulentic et al. (2007). Criteria employed in the present paper are also discussed in Negrete et al. (2014) and entail the following: (1) line widths of $\text{AlIII}\lambda 1860$ and $\text{SiII}\lambda 1814$

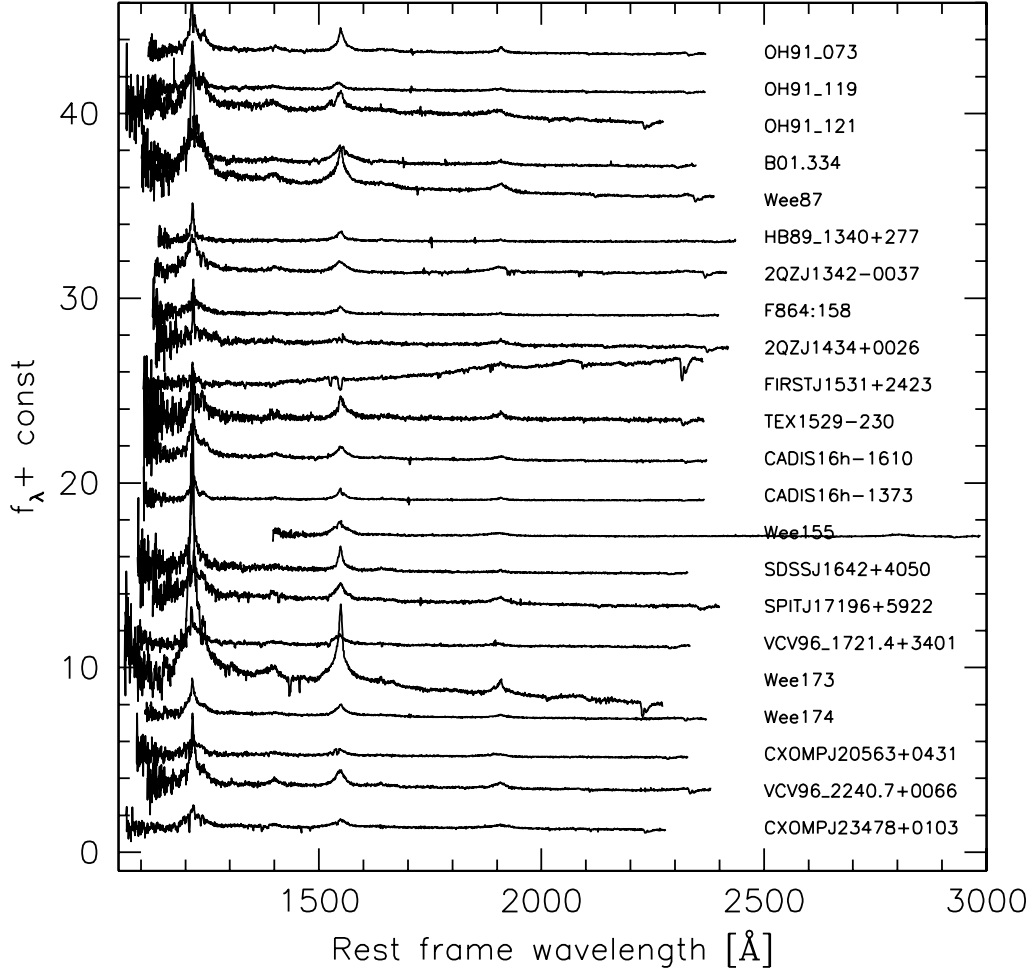


Fig. 3. GTC quasar spectra after redshift correction. Abscissa is the rest-frame wavelength in \AA , ordinate is the specific flux in units of $10^{-15} \text{ erg s}^{-1} \text{ cm}^{-2} \text{ \AA}^{-1}$. Spectra have been vertically displaced by adding steps of $\Delta f_\lambda = 2$ (no step was added for Wee 173 to avoid confusion with VCV96 from bottom to top).

Table 2. Log of observations.

QSO identification	Date Observation	ET Time (s)	Exp. N.	it S/N at 1450 \AA	Slit width (arcsecs)	seeing (arcsecs)
[OH91] 073	26-03-2011	2400	4	14	1.0	1.55
[OH91] 119	26-03-2011	2400	4	10	1.0	1.3
[OH91] 121	07-04-2011	2400	4	20	1.0	1.0
B1.0334	07-04-2011	2400	4	10	1.0	1.15
Wee 87	07-04-2011	2400	4	30	1.0	0.99
[HB89] 1340+277	02-05-2013	2400	4	5	1.0	1.0
2QZ J134206.3-003702	02-05-2011	2400	4	12	1.0	0.98
F864:158	06-05-2011	2400	4	5	1.0	1.3
2QZJ143400.0+002649	05-05-2013	2600	4	11	1.23	1.27
FIRST J153150.46+242317.7	02-05-2011	2400	4	9	1.0	0.80
TEX 1529-230	07-06-2011	2400	4	6	1.0	1.56
CADIS 16h-1610	08-07-2013	3250	5	12	1.23	0.97
CADIS 16h-1373	14-06-2013	3250	5	10	1.23	0.82
Wee 155	02-05-2011	2400	4	5	1.0	1.10
SSDS J164226.90+405034.3	08-04-2011	2400	4	6	1.0	1.25
SPIT 17196+5922	06-04-2011	2400	4	11	1.0	1.01
[VCV96] 1721.4+3401	06-05-2013	2600	4	7	1.23	1.15
Wee 173	05-05-2013	2600	4	40	1.23	0.99
Wee 174	11-06-2013	2600	4	21	0.8	1.2
CXOMP J205620.5-043100	04-07-2011	2400	4	8	1.0	1.15
[VCV96] 2240.7+0066	03-07-2011	2400	4	14	1.0	1.20
CXOMP J234752.5+010306	11-06-2013	2600	4	12	0.8	0.8

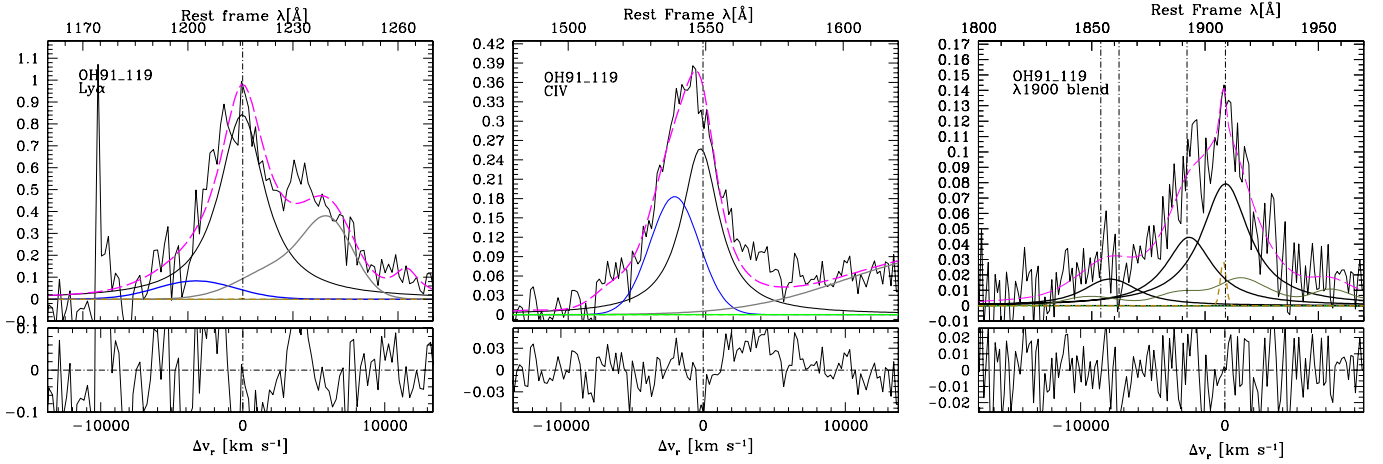


Fig. 4. Example of line-fit analysis results on the $\text{Ly}\alpha$ (left panel) $\text{CIV}\lambda 1549$ (middle) and 1900 \AA emission features for population A sources. The lines are shown after continuum subtraction. The magenta dashed line shows the full model of the emission features and intervening narrow absorptions, if present. The thick black lines show the broad components of the prominent emission lines. The thick blue line traces the BLUE component. The $\text{NV}\lambda 1240$ line on the red side of the $\text{Ly}\alpha$ profile is traced by a gray line that includes BC and BLUE. Orange lines are narrow-line components. The lower panel of each frame shows the residuals between the line model and the observations as a function of radial velocity from rest frame (for $\text{CIII}\lambda 1909$ in the case of the 1900 \AA blend). The complete figure for all population A sources is available in the electronic edition of the journal.

are found to be correlated with the $\text{H}\beta$ line width (Negrete et al. 2013a,b), which makes them useful virial estimators as well as suitable to distinguish populations A and B; (2) EW $\text{CIV}\lambda 1549$ values for population A1 and B sources are a factor of two higher than for the rest of the population A sources; and (3) blue and red $\text{CIV}\lambda 1549$ profile asymmetries appear to be signatures of population A and B sources, respectively. The criteria allow a reasonable separation of populations A and B. Those near the intersection (bin A1) are much less certain, and the bin probably is a mix of A and B sources. The fact that we find an even division between source populations (11 population A and 9 population B), as has been found at low redshift (Zamfir et al. 2010), suggests that our sample is a reasonably random selection of quasars in the context of 4DE1 (in Zamfir et al. 2010 the magnitude-limited SDSS sample divides 45% and 55% for populations A and B).

The intensity and profile of the emission lines were measured following the approach described in Marziani et al. (2010) and Negrete et al. (2013a). The salient assumption is that each line in a population A source can be interpreted as a composite of an unshifted symmetric component plus a blueshifted, asymmetric component (BLUE) related to systematic outflow motions. For population B sources any blueshifted component is much weaker, but a very broad and redshifted component (VBC) is usually seen along with the unshifted component that is assumed to arise in a virialized medium (the “classical” broad component; BC). These line components (BLUE, BC, and VBC) were included in modeling the strongest emission lines $\text{Ly}\alpha$, $\text{NV}\lambda 1240$, $\text{CIV}\lambda 1549$, $\text{HeII}\lambda 1640$, $\text{AlIII}\lambda 1860$, $\text{SiIII}\lambda 1892$, and $\text{CIII}\lambda 1909$. They were simultaneously fit along with the continuum and $\text{FeII} + \text{FeIII}$ emission (the latter is only relevant in the 1900 \AA blend and for population A). For the UV FeII and FeIII emissions we considered the templates provided by Brühweiler & Verner (2008) and Vestergaard & Wilkes (2001), respectively. The fitting routine scaled and broadened the original templates to reproduce the observed emission. FeII was always set to zero by the fitting routine, which reflects its low intensity and the low S/N in the observed spectral range. The S/N of some spectra allow only a marginal fit, with the greatest uncertainty involving the 1900 \AA blend and the blue component in population B sources.

The 1900 \AA blend has become important for several reasons: 1) FWHM $\text{AlIII}\lambda 1860$ and $\text{SiIII}\lambda 1892$ can be used as a virial estimator (Negrete et al. 2013a), and their FWHM can also be used for distinguishing population A and B sources; 2) the relative strength of $\text{AlIII}\lambda 1860$, $\text{SiIII}\lambda 1892$, and $\text{CIII}\lambda 1909$ can be used as additional diagnostics for distinguishing between population A and B quasars (Bachev et al. 2004; Negrete et al. 2013a); 3) line ratios involving $\text{SiIII}\lambda 1892/\text{CIV}\lambda 1549$ and $\text{AlIII}\lambda 1860/\text{SiIII}\lambda 1892$ are important for constraining the BLR physical conditions that can be used to estimate the BLR radius (Negrete et al. 2013a). The key is to use spectra with a high enough S/N to allow modeling and decomposing the lines in the blend.

Figures 3–5 show deredshifted spectra and individual fits for our GTC sample where S/N varies from 5–6 to 40. It is easy to see how the blend modeling becomes less certain for the examples with the lowest S/N.

2.4. Low-redshift comparison sample of luminosity analogs

The significance of observations for high z low luminosity quasars can be fully understood only if a suitable low- z control sample exists for the same luminosity range. Archived HST/FOS observations provide spectra with similar dispersion, S/N, and luminosity. The archival spectra were previously studied in the 4DE1 context (Bachev et al. 2004; Sulentic et al. 2007). The heterogeneous nature of both the GTC/OSIRIS and HST/FOS samples means that neither is complete.

The FOS sample in particular is strongly biased toward radio loud sources. We randomly extracted smaller subsamples that satisfy the following conditions: (1) the absolute magnitude distribution is not statistically different from that of the GTC sample; and (2) a consistent fraction of radio sources ($\approx 10\%$ as in the GTC sample). In practice, sources were selected from the sample of 130 sources given in Tables 1 and 2 of Sulentic et al. (2007), which are available at Vizier¹ in the absolute magnitude range $-25 \lesssim M_V \lesssim -23$. This yielded 42 sources, of which 23 were

¹ J/ApJ/666/757/CIVlines at <http://vizier.u-strasbg.fr/>

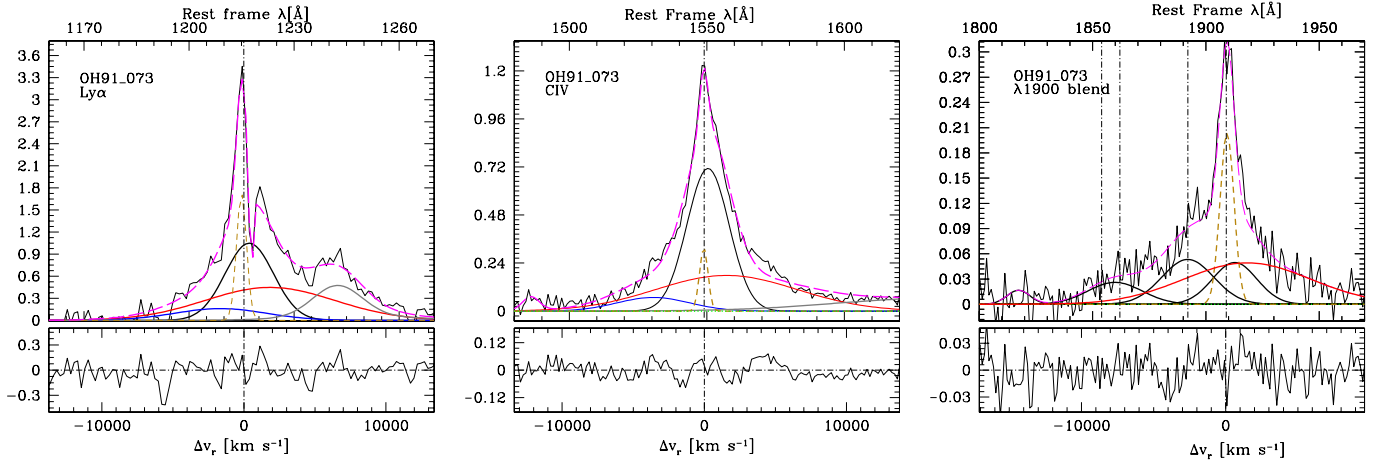


Fig. 5. Example of line-fit analysis results on the $\text{Ly}\alpha$ (left panel) $\text{CIV}\lambda 1549$ (middle) and 1900 \AA emission features for population B sources. The meanings of symbols and colors is as in the previous figure. The VBC assumed to be present in the population B emission line profiles is traced by a thick red line. The complete figure for all population B sources is available in the electronic edition of the journal.

Table 3. Measured quantities.

NED identification	f_λ^a	δf_λ	$\text{Ly}\alpha$		NV	$\text{OIV}] + \text{SiIV}$	$\text{CIV}\lambda 1549$			AlIII	$\text{SiIII}]$	$\text{CIII}]$	$\lambda 1900$
			$W [\text{\AA}]^b$	F^c	F^c	F^c	$W [\text{\AA}]^b$	F^c	F_{blue}/F	F^c	F^c	F^c	F^c
Population A													
OH91 119	0.35	0.04	58	23.3	9.6	4.0	36	10.8	0.38	0.7	1.8	3.2	5.7
OH91 121	1.24	0.06	55	80.4	23.9	14.0	37	42.5	0.20	3.5	9.6	5.6	18.8
Wee 87	1.29	0.06	90	153.3	27.0	10.5	51	59.8	0.09	2.7	5.4	13.8	21.9
F864:158	0.16	0.03	137	27.4	5.9	2.0	72	11.2	0.20	0.5	1.1	1.8	3.4
2QZ J143400.0+002649	0.61	0.06	68	52.1	7.9	4.4	26	15.6	0.11	1.1	4.4	4.5	10.0
SPIT 17196+5922	0.76	0.07	66	65.5	16.2	6.0	48	32.3	0.11	2.0	5.1	7.8	14.9
Wee 173	2.36	0.21	89	261.7	34.0	17.0	44	100.5	0.09	1.0	6.4	15.9	23.3
Wee 174	0.44	0.02	70	37.4	7.8	3.6	47	19.7	0.06	0.2	1.3	4.0	5.5
CXOMP J205620.5-043100	0.26	0.04	89	24.8	8.8	4.3	51	12.9	0.31	1.7	4.1	2.8	8.6
VCV96 2240.7+0066	0.66	0.05	101	73.7	11.1	8.0	50	29.6	0.19	1.5	3.2	8.2	13.0
CXOMP J234752.5+010306	0.36	0.03	144	49.9	4.8	2.9	46	17.4	0.10	1.8	2.5	5.1	9.4
Population B													
OH91 073	0.41	0.03	87	44.1	10.2	6.8	75	27.4	0.08	1.0	1.5	4.7	10.6
B1.0334	0.40	0.05	73	41.9	9.6	7.6	118	39.0	0.14	1.1	1.5	5.2	11.8
HB89 1340+277	0.12	0.03	252	20.5	1.4	1.8	141	14.4	0.17	0.5	0.5	1.3	2.7
2QZ J134206.3-003702	0.48	0.04	72	47.7	6.5	6.1	47	19.9	0.20	2.8	3.4	8.5	18.9
TEX 1529-230	0.51	0.08	72	36.7	21.2	6.5	64	31.6	0.02	0.6	2.6	6.8	13.4
CADIS 16h-1610	0.38	0.03	77	42.2	9.3	6.8	59	19.5	0.10	1.4	2.6	5.4	11.8
CADIS 16h-1373	0.11	0.02	277	27.3	5.8	1.5	129	13.2	0.09	0.6	0.8	2.6	5.2
SDSS J164226.90+405034.3	0.31	0.06	132	60.1	4.2	2.9	79	19.4	0.07	0.3	0.7	1.3	2.8
VCV96 1721.4+3401	0.27	0.04	77	27.8	7.4	4.3	90	19.5	0.32	0.8	1.9	2.9	6.5

Notes. ^(a) Rest-frame specific flux at 1450 \AA in units of $10^{-15} \text{ erg s}^{-1} \text{ cm}^{-2} \text{ \AA}^{-1}$. ^(b) Rest-frame equivalent width in \AA . ^(c) Rest-frame flux in units of $10^{-15} \text{ erg s}^{-1} \text{ cm}^{-2}$.

radio quiet. To produce a control sample with an RL fraction closer to that found in optically selected samples we defined a pure RQ sample of 23 sources supplemented with 3 randomly selected RL sources, which yielded 26 sources in the control sample (the 26 low- z sample is hereafter referred to as the FOS-CS).

3. Results

Figures 4 and 5 show the results of the SPECFIT (Kriss 1994) analysis of the $\text{Ly}\alpha$, $\text{CIV}\lambda 1549$, and 1900 blends in individual population A and B sources of the GTC sample. Table 3 reports quantities measured in the rest-frame spectra of each source as follows: rest-frame continuum flux level at 1450 \AA and associated uncertainty; total fluxes for the most prominent broad emission features ($\text{Ly}\alpha$, $\text{NV}\lambda 1240$, $\text{OIV}] \lambda 1402 + \text{SiIV} \lambda 1397$,

$\text{CIV}\lambda 1549$, $\text{AlIII}\lambda 1860$, $\text{SiIII}] \lambda 1892$, $\text{CIII}] \lambda 1909$); equivalent widths for $\text{Ly}\alpha$ and $\text{CIV}\lambda 1549$ (equivalent widths for other lines can be estimated by scaling EW $\text{CIV}\lambda 1549$ by line $\text{CIV}\lambda 1549$ flux ratio). Data are presented in two groups: upper population A, and lower population B.

Our SPECFIT analysis followed past work of modeling $\text{H}\beta$ and $\text{CIV}\lambda 1549$, where the strongest results were obtained from studies of $\text{H}\beta$ (at $z < 0.7$) for which the largest body of data exists (Marziani et al. 2003, 2009; Zamfir et al. 2010). As noted in Sect. 2.3, past work identified three broad emission components (BLUE, BC, and VBC) that show different relative intensities in different sources and are not necessarily present in every individual line or source (Marziani et al. 2010). The classical relatively unshifted broad $\text{H}\beta$ component is present in almost all sources and is assumed to be the most reliable

Table 4. Measured CIV λ 1549 line profile quantities.

NED identification	$FWHM(CIV\lambda 1549)$ [km s $^{-1}$]	A.I.	Kurt.	$c(\frac{1}{4})$ [km s $^{-1}$]	$c(\frac{1}{2})$ [km s $^{-1}$]
Population A					
OH91 119	4510 \pm 260	-0.17 \pm 0.06	0.41 \pm 0.05	-1270 \pm 210	-1170 \pm 130
OH91 121	6990 \pm 370	-0.18 \pm 0.06	0.37 \pm 0.07	-1060 \pm 320	-1160 \pm 190
Wee 87	4610 \pm 390	-0.14 \pm 0.09	0.31 \pm 0.04	-390 \pm 360	-50 \pm 190
F864:158	4880 \pm 540	-0.26 \pm 0.07	0.28 \pm 0.04	-830 \pm 290	-380 \pm 270
2QZ J143400.0+002649	4800 \pm 930	-0.23 \pm 0.07	0.26 \pm 0.03	-1130 \pm 320	-500 \pm 470
SPIT 17196+5922	5160 \pm 400	-0.11 \pm 0.08	0.33 \pm 0.04	-480 \pm 340	-330 \pm 200
Wee 173	4230 \pm 350	-0.21 \pm 0.11	0.27 \pm 0.04	-1130 \pm 470	-310 \pm 170
Wee 174	5070 \pm 360	-0.04 \pm 0.08	0.34 \pm 0.04	-210 \pm 350	-200 \pm 180
CXOMP J205620.5-043100	6240 \pm 280	-0.07 \pm 0.06	0.49 \pm 0.04	-820 \pm 270	-950 \pm 140
VCV96 2240.7+0066	5300 \pm 340	-0.08 \pm 0.07	0.37 \pm 0.05	-490 \pm 310	-490 \pm 170
SDSS J234752.55+010305.0	5600 \pm 620	-0.19 \pm 0.08	0.28 \pm 0.03	-900 \pm 390	-260 \pm 310
Population B					
OH91 073	4170 \pm 250	-0.02 \pm 0.11	0.38 \pm 0.05	130 \pm 360	190 \pm 130
B1.0334	7580 \pm 580	0.08 \pm 0.09	0.31 \pm 0.04	530 \pm 650	-10 \pm 290
HB89 1340+277	4620 \pm 280	-0.13 \pm 0.18	0.35 \pm 0.07	-860 \pm 740	-360 \pm 140
SDSS J134206.34-003701.2	6880 \pm 440	0.00 \pm 0.07	0.38 \pm 0.04	-220 \pm 410	-250 \pm 220
TEX 1529-230	5840 \pm 340	0.11 \pm 0.10	0.39 \pm 0.05	1040 \pm 490	640 \pm 170
CADIS 16h-1610	5930 \pm 340	-0.03 \pm 0.08	0.40 \pm 0.05	10 \pm 370	110 \pm 170
CADIS 16h-1373	5460 \pm 310	-0.01 \pm 0.08	0.41 \pm 0.05	-10 \pm 310	40 \pm 150
SDSS J164226.90+405034.3	3180 \pm 180	0.00 \pm 0.07	0.42 \pm 0.04	-100 \pm 180	-110 \pm 90
VCV96 1721.4+3401	8740 \pm 490	0.12 \pm 0.06	0.43 \pm 0.04	-120 \pm 410	-650 \pm 240

virial estimator after MgII λ 2800 (Marziani et al. 2013). This is where the population A–B distinction becomes important. Population A sources involving the highest L/L_{Edd} emitters show a Lorentzian BC component with a FWHM of ≤ 4000 km s $^{-1}$, plus, in extreme sources, a component on the blue side of the BC. Population B sources, including most radio-loud quasars, show a BC and a broader redshifted VBC component. In a few cases we suspect that the H β profile may be dominated by the VBC (e.g., PG 1416–129; Sulentic et al. (2000c)). Detailed studies of the CIV λ 1549 profile in low- z quasars are more limited and rely on the ≈ 140 sources with HST archival spectra (Bachev et al. 2004; Sulentic et al. 2007). Population A sources show a stronger CIV λ 1549 blue component, which can be much stronger than the BC (no VBC emission is seen). The well-studied NLSy1 source IZw1 is a population A (bin A3) prototype. In some sources a red asymmetry is seen in the CIV profile and is attributed to VBC emission – almost always involving population B sources.

The estimated contribution of the blue component to the total flux of CIV λ 1549 is listed in Table 3 in the column labeled F_{blue}/F . Table 4 reports quantities measured from the full broad line profiles (i.e., without separating line components). The other columns of Table 4 list the FWHM CIV λ 1549 and other profile-shape parameters that provide a quantitative description of CIV λ 1549 (see Zamfir et al. 2010 for definitions): asymmetry index, kurtosis, and centroid displacement (with respect to the rest frame) at one quarter and half of the fractional intensity.

While we applied our standard multicomponent SPECFIT analysis to all GTC spectra, the S/N of the data make clear that we might be over-interpreting some of the spectra. We show all individual fits and table-derived quantities, even though some are uncertain and not directly relevant to the goals of the paper, which involve high- and low-redshift comparisons for population A and B quasars. Subtraction of a blue component from CIV λ 1549 is well supported for population A sources, which also show a mean profile blueshift of ~ 450 km s $^{-1}$. However, population B sources show no systematic blueshift, which makes us doubt the reality of a blue component in these sources. The

modeling of broader population B line profiles is always more problematic. For the population A sources the presence of blue and BC components is well established and no evidence of a VBC is found.

3.1. CIV λ 1549 in populations A and B at high and low redshift

CIV λ 1549 is the safest feature with which to effect a comparison between low and high redshift. CIV λ 1549 is a strong collisional resonance doublet and is not heavily blended with other strong lines. The CIV λ 1549 profile shift was chosen as a principal 4DE1 parameter because it showed a strong population A–B difference. EW CIV λ 1549 and the CIV λ 1549 profile asymmetry can also serve as 4DE1 diagnostics (Sulentic et al. 2007). Table 5 reports the virial broadening estimator FWHM (see Sect. 3.4) and measurements of the CIV λ 1549 line profile (FWHM, asymmetry index, kurtosis, and centroids at one quarter and half maximum; see Zamfir et al. 2010 for definitions of parameters given here) for the GTC and B04 composites.

CIV λ 1549 shows a striking similarity at high and low redshift in populations A and B. The composite spectra show the median equivalent width (EW), asymmetry index (AI) and profile shift at half maximum ($c(\frac{1}{2})$) at low and high z that are almost identical (Tables 5 and 6). We were able to distinguish populations A and B on the basis of the same criteria as were employed at low z applied to the UV (Sect. 2.3 and Negrete et al. 2014), and quantitative population A–B differences in EW and profile measurements previously found at low redshift are confirmed in the high-redshift GTC sample. CIV λ 1549 in population A sources shows a systematically lower EW than population B, as well as blue asymmetric and blueshifted profiles. Population B sources show a stronger high-ionization spectrum without evidence for profile blueshifts/asymmetries. Population B shows an additional very broad and redshifted component with FWHM and shift values similar to those found for H β at low redshift.

Figure 6 compares the CIV λ 1549 equivalent width, centroid shift, and FWHM distributions for the high- and low-redshift

Table 5. Measured line profile quantities of composite spectra.

Identification	Virial FWHM ^a [km s ⁻¹]	FWHM(CIV λ 1549) ^b [km s ⁻¹]	A.I. ^c	Kurt. ^c	$c(\frac{1}{4})^c$ [km s ⁻¹]	$c(\frac{1}{2})^c$ [km s ⁻¹]
Pop. A average	3470:	5220 \pm 430	-0.12 \pm 0.08	0.32 \pm 0.04	-730 \pm 370	-440 \pm 220
Pop. B average	5080	6290 \pm 380	0.01 \pm 0.09	0.39 \pm 0.05	10 \pm 460	-20 \pm 190
Pop. A median	2880 \pm 320 ^a	5010 \pm 390	-0.10 \pm 0.10	0.31 \pm 0.04	-570 \pm 430	-270 \pm 200
Pop. B median	4430	5830 \pm 350	0.02 \pm 0.10	0.38 \pm 0.05	350 \pm 450	270 \pm 170
Pop. A B04	2430 \pm 100	4060 \pm 400	-0.15 \pm 0.09	0.31 \pm 0.04	-770 \pm 310	-500 \pm 200
Pop. B B04	4300	5810 \pm 450	0.00 \pm 0.12	0.36 \pm 0.06	10 \pm 590	-10 \pm 230

Notes. ^(a) Virial FWHM measured on AlIII λ 1860 and SiIII] λ 1892 in accordance with the finding of Negrete et al. (2013a). The uncertainty is the standard deviation computed on the two lines FWHM. If no uncertainty is given, the fit was obtained with the same FWHM value for both AlIII λ 1860 and SiIII] λ 1892. ^(b) FWHM of the CIV λ 1549 line measured on the full profile, i.e., including BC and VBC and BLUE when appropriate. ^(c) Measurements of the CIV λ 1549 full line-profile asymmetry index, kurtosis, and centroids at one quarter and half maximum on; see Zamfir et al. (2010) for definitions of parameters.

Table 6. Measured quantities of composite spectra.

Identification	Ly α		Nv	OIV]+Siiv	CIV λ 1549			AlIII	SiIII]	CIII]	λ 1900
	W [Å] ^b	F ^c			F ^c	F ^c	W [Å] ^b				
Pop. A average	78	87	19.1	8.4	46	42.9	0.10	1.9	7.3	8.5	17.7
Pop. B average	84	103.0	38.3	13.9	77	69.3	0.09	3.6	7.0	13.3	30.5
Pop. A median	74	80.0	16.7	9.0	45	42.7	0.18	1.8	5.8	6.6	14.1
Pop. B median	121	131.5	26	13.0	69	62.2	0.07	3.1	3.9	14.5	26.0
Pop. A B04	87	107.7	15	13.9	51	49.7	0.13	2.5	5.4	11.4	19.3
Pop. B B04	95	115.9	27	11.5	83	77.5	0.11	2.6	3.5	13.0	23.5

Notes. ^(a) Rest-frame specific flux at 1450 Å in units of erg s⁻¹ cm⁻² Å⁻¹. ^(b) Rest-frame equivalent width in Å. ^(c) Rest-frame flux in units of erg s⁻¹ cm⁻².

samples. Populations A and B are identified. Low-redshift samples (Bachev et al. 2004; Sulentic et al. 2007) show lower population A equivalent widths values than population B ($W(\text{CIV}\lambda 1549)_A \approx 50$ Å vs. $W(\text{CIV}\lambda 1549)_B \approx 100$ Å). Our high-redshift sample shows $W(\text{CIV}\lambda 1549)_A \approx 47$ Å vs. $W(\text{CIV}\lambda 1549)_B \approx 79$ Å similar to the differences found at low redshift, where population A sources generally show a weaker high-ionization line spectrum (Marziani et al. 2001, 2010). Note that there is again no significant difference between the $W(\text{CIV}\lambda 1549)$ values between the GTC and FOS-CS. The distribution of Fig. 6 shows a few (1–3, depending on the random selection of radio sources) large equivalent width sources in the FOS-CS that have no correspondence in the GTC sample. They are not numerous enough to make the samples significantly different. Median FWHM(CIV λ 1549) measurements for the high-redshift sample are 5070 km s⁻¹ and 5840 km s⁻¹ for populations A and B, which is roughly consistent with the low- z FOS-CS. However, there is a small discrepancy involving the FWHM CIV λ 1549 comparison, where the high- z populations A and B average composite widths are about 28% and 8% broader than those of the B04 composites. These differences are not statistically significant – given the small sample size and the errors involved. The difference disappears for population B if medians are considered, and is reduced to $\approx 23\%$ for population A. Analogous considerations apply to the virial FWHM.

Considering the individual and composite fits to the CIV λ 1549 profile, we do not confirm a near ubiquity of blueshifts or asymmetries for type 1 quasars (Richards et al. 2011), but rather the same population A/B dichotomy as is seen at low redshift (Sulentic et al. 2007), where population B

sources show redshifts and asymmetries or symmetric unshifted profiles.

3.2. Comparing population A and B UV spectra at high and low redshifts

A comparison of population A and B sources at high and low redshift cannot extend beyond the CIV λ 1549 line without using composite spectra to enhance the spectral S/N. The GTC sample is not large enough ($N = 20$) to permit a fine subdivision, therefore we simply constructed the population A and B median composites that are shown in the upper panel of Fig. 7, which involves 11 population A and 9 population B sources.

The best low- z composites come from Bachev et al. (2004). This sample was large enough to permit constructing composite spectra for each of the five most populated 4DE1 bins (Sulentic et al. 2002). The bin composites were then combined to produce two higher S/N composites for populations A and B. Low- z population A and B composites shown in the bottom panel of Fig. 7 were obtained by weighting sources from the five spectral subtypes by their relative frequency in the sample. These weighted-average composites include all Bachev et al. (2004) spectra. They are the best control-sample composites, but include many sources that fall outside the narrow luminosity range (almost all lower) of our GTC sample. To check these composites we also generated (lower S/N) composites from our luminosity-restricted FOS-CS control sample taken from Sulentic et al. (2007). The samples of Bachev et al. (2004) and Sulentic et al. (2007) are largely overlapping with that of Bachev et al. (2004), which includes 139 sources vs.

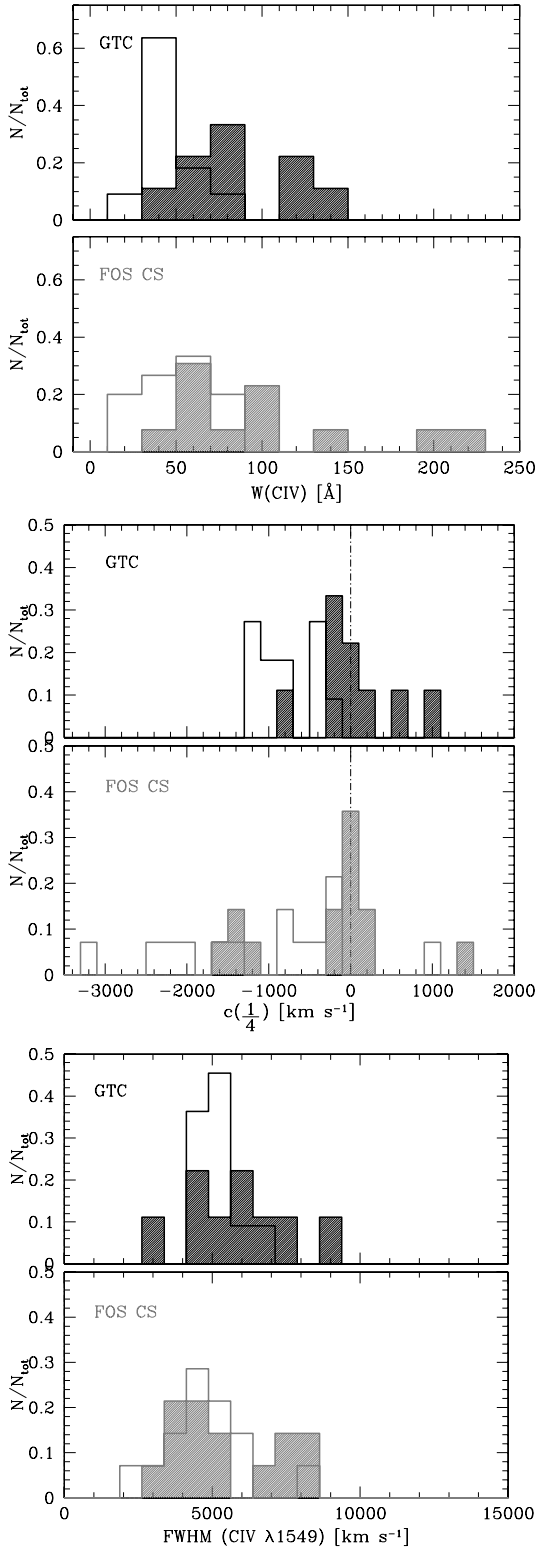


Fig. 6. *Top to bottom:* distributions of $W(\text{CIV}\lambda 1549)$ for GTC (upper panel; black) and one realization of the FOS CS (gray). The shaded histogram refers to population B sources. *Middle:* the same for the distributions of $c(\frac{1}{4})$; *bottom:* the same for the distributions of $\text{FWHM}(\text{CIV}\lambda 1549)$.

130 of [Sulentic et al. \(2007\)](#). The 26 sources of CS are included in both samples. The luminosity-restricted FOS-CS composites show no major differences from those obtained from the less restricted [Bachev et al. \(2004\)](#) composites. Neither FOS-CS composite (except for slightly weaker $\text{NIII}]\lambda 1750$ emission in

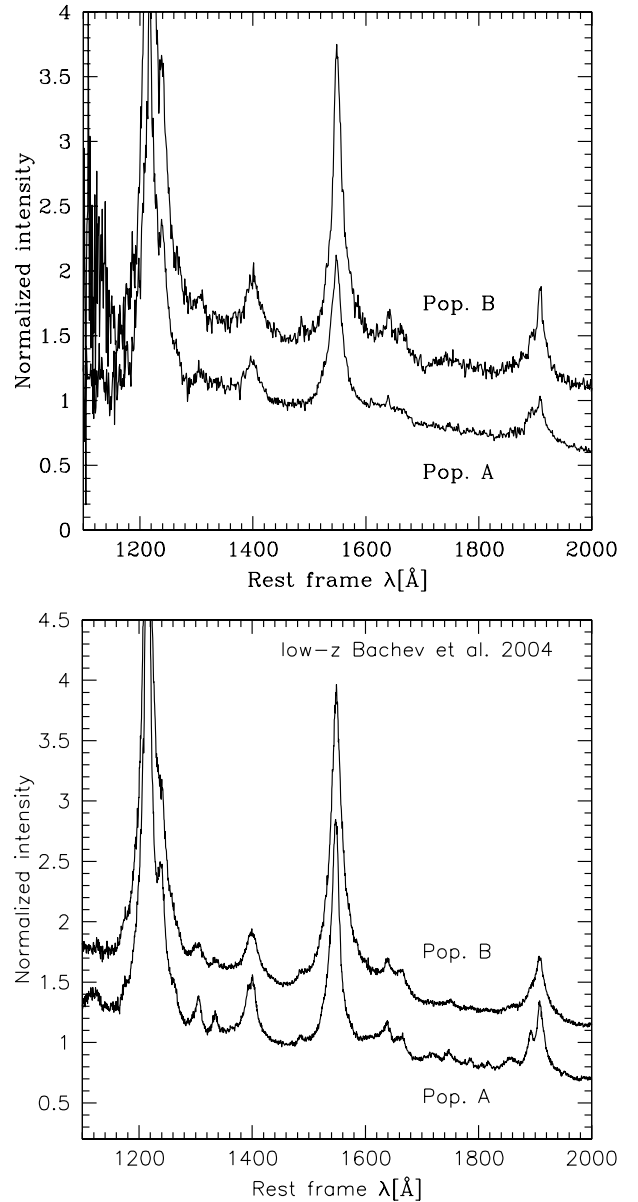


Fig. 7. Population A and B median spectra for the present GTC sample and for the low- z sample of [Bachev et al. \(2004; bottom\)](#).

population A). We therefore cautiously adopted the composites of [Bachev et al. \(2004\)](#) for all comparisons; these composites have a higher S/N. The two bottom rows of Fig. 8 (the panels labeled B04) present results from the SPECFIT analysis of the low- z composites of [Bachev et al. \(2004\)](#) for $\text{Ly}\alpha$, $\text{CIV}\lambda 1549$, and the 1900 blend, and the last two rows of Table 6 report measurements derived from this analysis (last two rows identified with the label B04).

If one assumes that source luminosity is the principal driver of quasar structure and kinematics, we expect our low- z and GTC composites to be very similar. Our work in the 4DE1 context suggests that L/L_{Edd} is the principal driver ([Marziani et al. 2001](#)). A comparison of this kind requires that populations A and B are separated because quasar spectra are *not* the same and spectral differences at any fixed redshift are maximized using the population A and B distinction, which is driven by L/L_{Edd} . We are not aware of a more effective distinction. Previous work on low-redshift samples show that the two populations divide approximately 60%/40%, with RQ/RL quasars dividing 90%/10%,

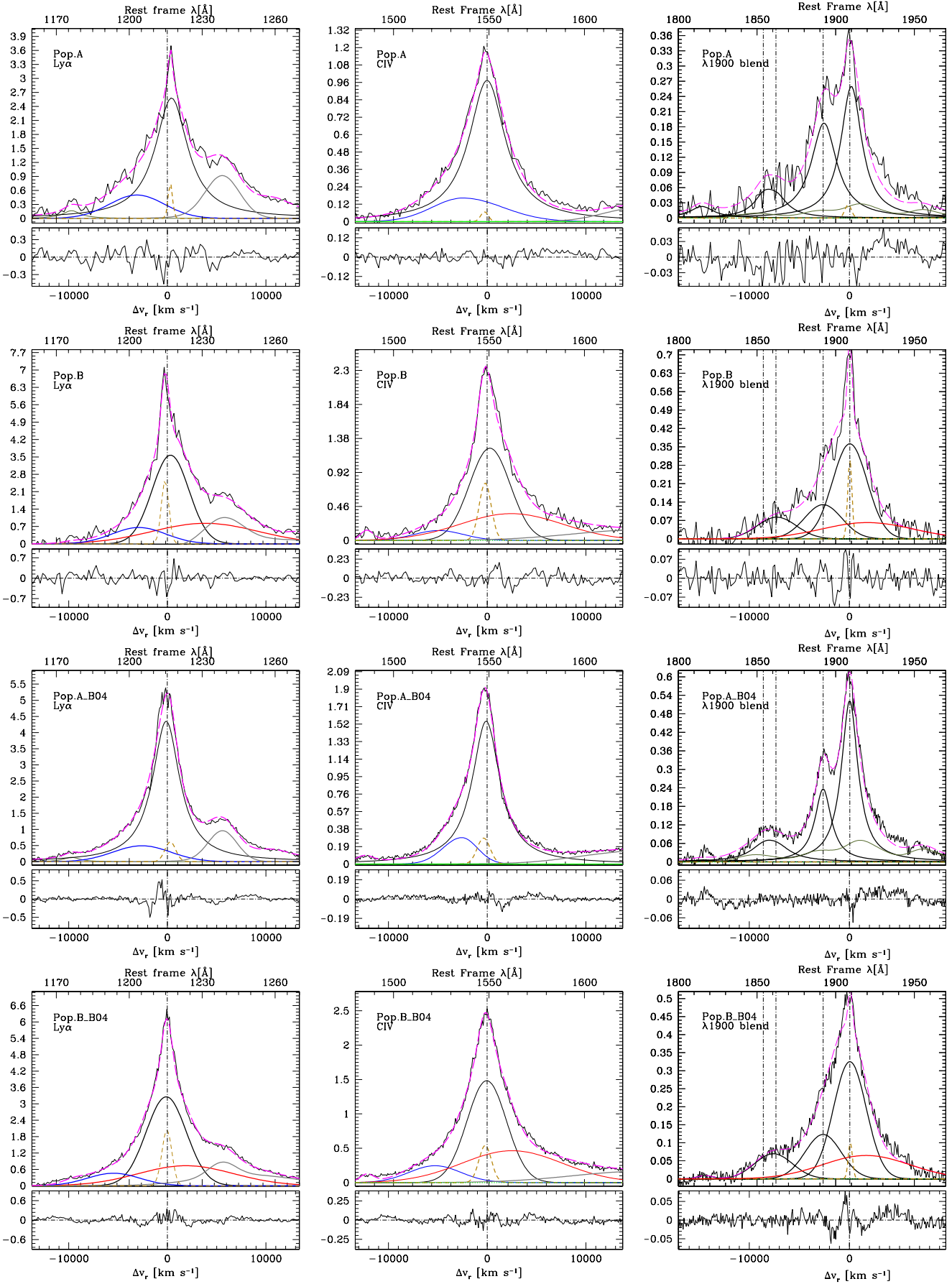


Fig. 8. Fits to the emission lines in Population A and B GTC median spectra. The two lower panels show the same analysis for the [Bachev et al. \(2004\)](#) median composites. The meaning of colors and symbols is the same as that in Figs. 4 and 5.

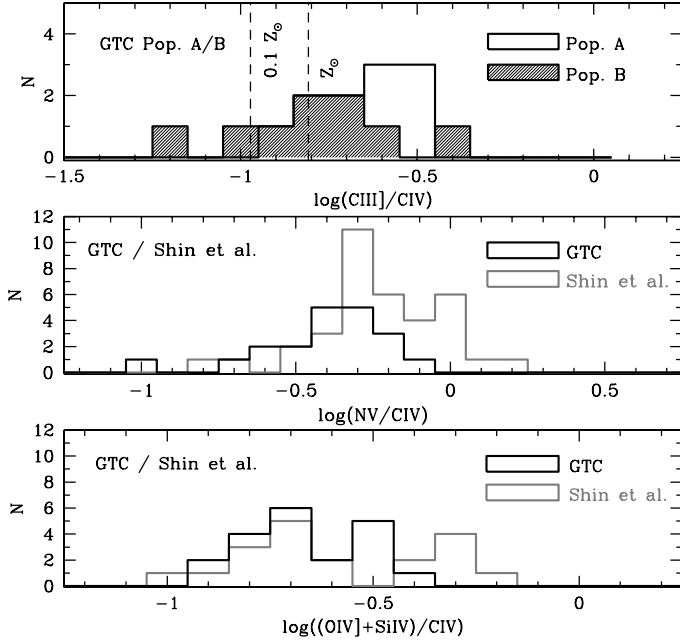


Fig. 9. Distributions of Z-sensitive ratios. *From top to bottom:* CIII] λ 1909/CIV] λ 1549 for the GTC sample (the dashed histogram is for population B). Dot-dashed lines trace the expected ratios for $Z = 0.1 Z_{\odot}$ and $Z = Z_{\odot}$ for $\log n_{\text{H}} = 10$ and $\log U = -1.75$. *Middle:* distribution of the ratio NV] λ 1240/CIV] λ 1549 for the GTC (black lines) and the Shin et al. (2013) low- z sample (gray lines), with the restriction $\log L \geq 46.2$ [erg s $^{-1}$]. *Bottom:* the same for the ratio (OIV] λ 1402+SiIV] λ 1397)/CIV] λ 1549.

and the wide majority of RLs belonging to population B (Zamfir et al. 2008). If our samples are small or modest as in the present case, an over-representation of extreme sources would bias the comparison. There is no reason to expect (and no evidence for) such an over-representation. If, for example, many of our sources were soft X-ray selected, we would expect them to preferentially occupy 4DE1 spectral bins A2, A3, and A4, which also show the highest and most frequent CIV] λ 1549 blueshifts (smallest M_{BH} and highest L/L_{Edd}). Radio-selected quasars would largely occupy population B spectral bins. Table 1 suggests that few of our quasars were selected in either way. If they favor something at all, deep optical grism searches will favor quasars with stronger (broader, higher EW) spectral lines. This might disfavor extreme population A quasars, and indeed, we find only two candidate extreme population A sources (i.e., narrow-line Seyfert 1) in the GTC sample (Q1232-1113 and CXOMPJ20563-0431). Because they are hypothesized to be younger quasars, we might expect to find more of them at $z \approx 2.3$. High- z analogs of I Zw 1 (albeit with a much higher luminosity) were identified in one of our companion surveys (Dultzin et al. 2011; Negrete et al. 2012; Marziani & Sulentic 2014a,b).

Table 6 reports normalized fluxes and equivalent widths for population A and B composite spectra (average and median). The spectra are shown in Fig. 7. Note that the measurements come from the composite spectra using the same SPECFIT analysis (Fig. 8, top rows) as was applied to individual sources. Given the sizes of both samples, some differences due to outlying or peculiar sources might affect the average values or composites, but the mean and median composites yield values that are mutually consistent. The values for population A and B composite spectra are consistent with the values derived for the 11 and 9 individual spectra.

In conclusion, following the 4DE1 formalism, we attempted a first-order separation of our high- z and low- z samples into population A and B quasars. In the UV rest wavelength range studied here we find evidence for spectral differences between population A and B, especially in measurements of CIV], which is strong and not blended with other strong lines. Table 6 compares high- and low-redshift median composite spectra for populations A and B. Both low- and high- z population B samples show stronger high-ionization spectra and stronger narrow lines than population A, while no major difference is found between GTC and the B04 composites.

3.3. Metallicity difference between high and low z ?

One advantage of comparisons involving UV spectra is that they provide several line ratios that can serve as metallicity indicators. Most results of the past decade point toward solar and supersolar metallicity even at very high redshifts (e.g., Hamann & Ferland 1993; Kurk et al. 2007; Willott et al. 2010). Of course these studies involved extremely luminous sources. The GTC sample spectra have a high enough S/N to permit reasonable measurements of metallicity indicators (NV] λ 1240/CIV] λ 1549, SiIV] λ 1397+OIV] λ 1402/CIV] λ 1549). The ratio involving nitrogen and carbon scales with metallicity by virtue of the secondary enrichment of nitrogen in massive stars (Hamann & Ferland 1993; Hamann et al. 2002). The ratio SiIV] λ 1397+OIV] λ 1402/CIV] λ 1549 involves ionic species of two α elements relative to carbon. The dependence of SiIV] λ 1397+OIV] λ 1402/CIV] λ 1549 on Z has been calibrated by photoionization computations (Nagao et al. 2006b) and widely used in recent quasar studies involving metal abundances (e.g., Wang et al. 2012; Shin et al. 2013). The values of the ratios obtained from the fluxes in Table 3 indicate a wide spread (at least 0.6 dex) in both the NV] λ 1240/CIV] λ 1549 and (SiIV] λ 1397+OIV] λ 1402/CIV] λ 1549) ratios (middle and bottom panel of Fig. 9). The largest sample currently available for comparison is provided by Shin et al. (2013), who measured NV] λ 1240/CIV] λ 1549 and SiIV] λ 1397+OIV] λ 1402/CIV] λ 1549 from IUE and HST spectra of PG quasars available in the MAST archive. Figure 9 compares the GTC distribution of NV] λ 1240/CIV] λ 1549 (middle panel) and (SiIV] λ 1397+OIV] λ 1402/CIV] λ 1549 (lower panel) with those of Shin et al. (2013). Figure 10 compares GTC measurements for NV] λ 1240/CIV] λ 1549 (upper panel) and (SiIV] λ 1397+OIV] λ 1402/CIV] λ 1549 with those of Shin et al. (2013) as a function of source bolometric luminosity. The GTC sample overlaps the high- L part of the Shin et al. (2013) sample, where more metal-rich sources are found (Juarez et al. 2009). The correlation between Z-sensitive ratio NV] λ 1240/CIV] λ 1549 and L in Fig. 10 was reported previously (Nagao et al. 2006b), although its origin is unclear (Sect. 4.4). To make a meaningful comparison between the GTC and low- z samples we applied a restriction to luminosities higher than 10^{45} erg s $^{-1}$. In this case, there is a consistent difference in the ratio distribution, supported by K-S tests, in the sense that the GTC sample sources show lower values.

The metallicity is estimated to be solar or slightly subsolar in the lowest Z cases. We tentatively identify at least four quasars (F864-158, Q 1340+27, Q 1640+40 and CADIS 16h-1610) that appear to show subsolar or solar metallicities following the normalization of Nagao et al. (2006b). A low- Z for these sources is also suggested by their large CIV] λ 1549/CIII] λ 1909 ratios (upper panel of Fig. 9). This ratio is usually not considered as a metallicity indicator because it

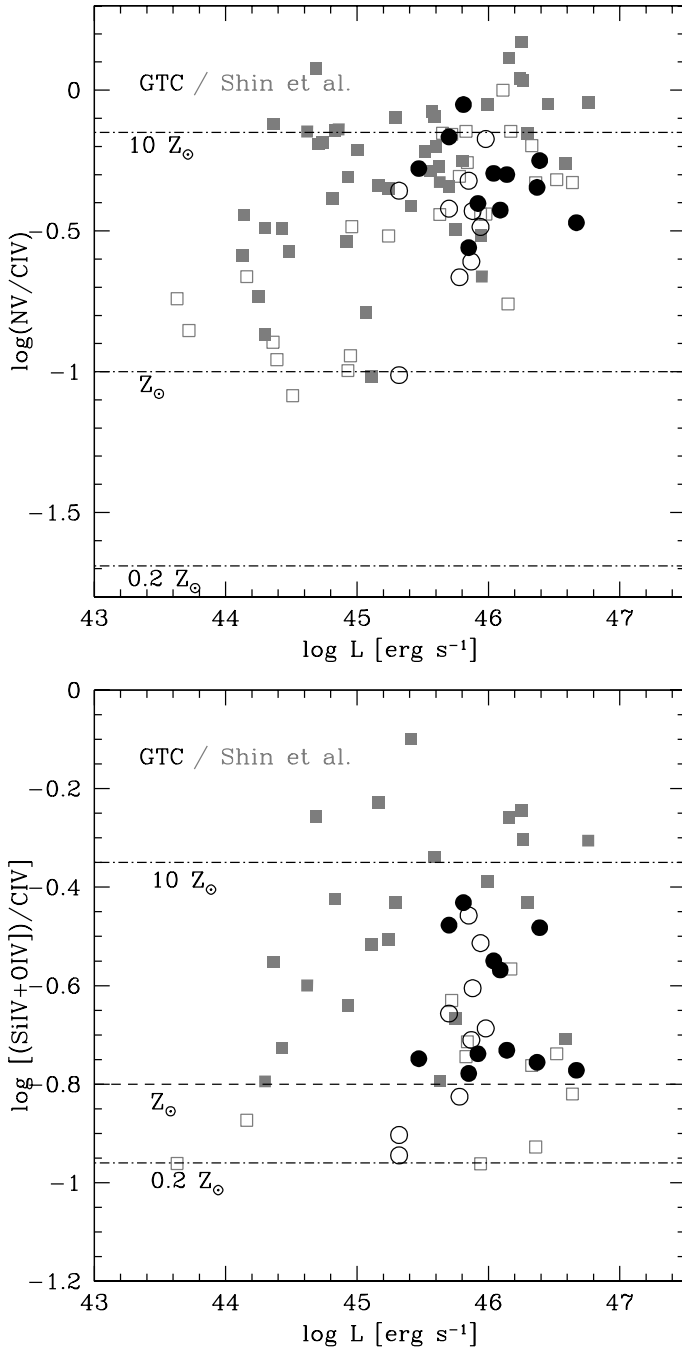


Fig. 10. Metallicity-sensitive line intensity ratios as a function of bolometric luminosity for the sample of Shin et al. (2013; gray squares) and the GTC sample (black circles). Open symbols are for population B sources, filled symbols for population A. The ordinate of the *top panel* is the decimal logarithm of the intensity ratio between $\text{NV}\lambda 1240$ and $\text{CIV}\lambda 1549$; the ordinate of the *bottom panel* is the decimal logarithm of the intensity ratio of the 1400 Å blend due to multiplets of SiIV and OIV , and $\text{CIV}\lambda 1549$. The dashed lines show the value expected for 0.2, 1, and 10 times solar metallicity following the LOC models reported in Nagao et al. (2006b).

is sensitive to ionization level, density (the $\text{CIII}\lambda 1909$ line is emitted in an inter-combination transition with a well-defined critical density), and because it is the ratio between lines of two different ionic species of the same element. However, for a fixed density (below the critical density of $\text{CIII}\lambda 1909$) and ionization parameter, CLOUDY (Ferland et al. 2013)

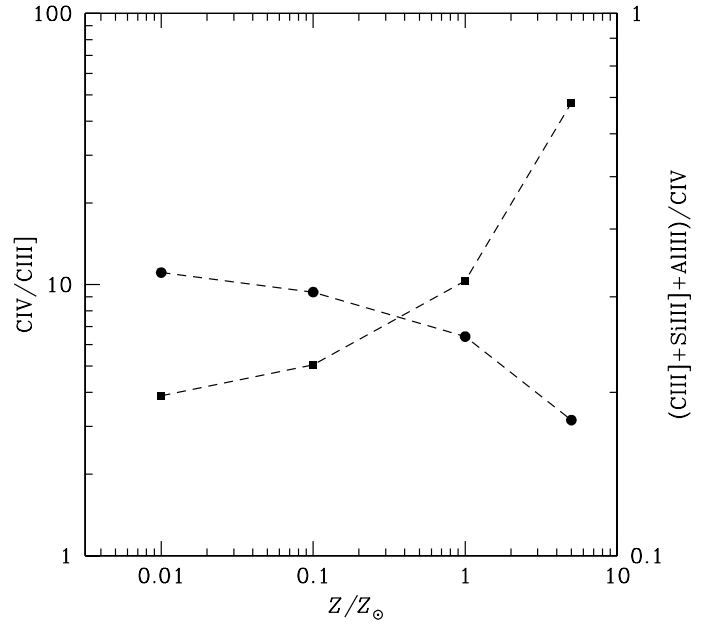


Fig. 11. Line-intensity ratios $\text{CIV}\lambda 1549/\text{CIII}\lambda 1909$ (filled circles) and total 1900 blend/ $\text{CIV}\lambda 1549$ (filled squares), for four values of Z , 0.01, 0.1, 1, 5 times solar, computed for $\log U = -1.75$ and $\log n_{\text{H}} = 10$.

photoionization simulations show a remarkable dependence on metallicity for the ratios $\text{CIII}\lambda 1909/\text{CIV}\lambda 1549$ and $(\text{AlIII}\lambda 1860 + \text{SiIII}\lambda 1892 + \text{CIII}\lambda 1909)/\text{CIII}\lambda 1909$ (Fig. 11). These trends are explained by an increase of electron temperature with decreasing metallicity: at $Z \sim 0.01 Z_{\odot}$, $T_e \approx 27\,000$ K, at $Z \sim 5 Z_{\odot}$, $T_e \approx 16\,000$ (assuming $\log U = -1.75$ $\log n_{\text{H}} = 10$). The higher T_e , due to a lower cooling rate of the BLR at low Z , increases the collisional excitation rate of $\text{CIV}\lambda 1549$ and therefore favors this line over lower excitation metal lines. It is interesting to note that this interpretation is analogous to ascribing the change in $\text{OIII}\lambda 4959,5007$ strength in Galactic and extragalactic HII regions to differences in metal content (e.g., Searle 1971).

An additional line of evidence supports the idea of lower chemical abundance in GTC sources in population A. Figure 12 shows a comparison of the difference in line width of the population A composite spectra for GTC and FOS sources on an expanded scale to emphasize the weak lines. The low- z FOS composite is much richer in faint narrow and semibroad features. Two emission lines coming from two different ionic species of nitrogen are detected in quasar spectra: $\text{NIII}\lambda 1750$ and $\text{NIV}\lambda 1486$. We estimate an upper limit of ≈ 0.5 Å for $\text{NIV}\lambda 1486$ (the line is not visible) and $W(\text{NIII}\lambda 1750) \approx 0.6$ Å for the GTC median composite. Both lines are clearly seen in the low- z composites with $W(\text{NIV}\lambda 1486) \approx 0.8$ Å and $W(\text{NIII}\lambda 1750) \approx 1.6$ Å. The weakness or even absence of both of them in the GTC composites implies a lower nitrogen abundance in the high- z sources. The $\text{Si II}\lambda 1264$, $\text{OI}\lambda 1304$ and $\text{OIII}\lambda 1663$ lines (from α elements), as well as the Fe II UV 191 blend, are certainly detected in the FOS composite. The weaker UV 191 Fe II multiplet in the GTC spectrum points toward a clear role for excitation conditions and chemical abundance. Both standard diagnostic line ratios and the comparison of composites are evidence for a metallicity redshift gradient.

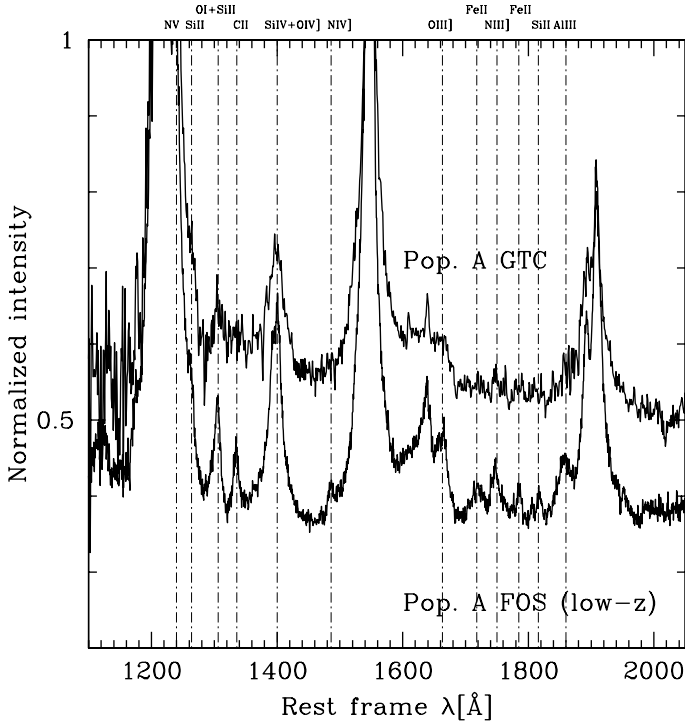


Fig. 12. Median spectra of population A for the GTC sample (*top*) and for the spectra for the low- z sample of Bachev et al. (2004; *bottom*). The continuum has been flattened and the intensity-limit cut set to emphasize faint features that are possibly related to differences in the metal content. The displacement of the two spectra is due to an artificial offset.

3.4. M_{BH} and L/L_{Edd} at high and low z

Our first attempt to estimate black hole masses and Eddington ratios revealed no significant difference between population A and B sources. We considered virial FWHM values for five UV lines ($\text{Ly}\alpha$, $\text{CIV}\lambda 1549$, $\text{AlIII}\lambda 1860$, $\text{SiIII}\lambda 1892$, and $\text{CIII}\lambda 1909$) as well as an average FWHM of all five lines. In a few cases not all the lines could be measured. The first line is dangerous for many reasons. The second is our strongest and least contaminated line, but different studies suggest it is not reliable as a virial estimator (Sulentic et al. 2007; Netzer et al. 2007). $\text{CIII}\lambda 1909$ is seriously blended, and similarly, the FWHM $\text{CIII}\lambda 1909$ shows no correlation with FWHM $\text{H}\beta$. Recent studies using high S/N spectra (Negrete et al. 2013a; Negrete et al. 2014) suggest that $\text{AlIII}\lambda 1860$ and $\text{SiIII}\lambda 1892$ are most likely the safest virial estimators in UV spectra of quasars. $\text{AlIII}\lambda 1860$ is preferred because it is on the blue edge of the $\lambda 1900$ emission line blend.

We do not report M_{BH} and L/L_{Edd} estimates for individual sources, but follow the procedure developed in Sulentic et al. (2002) and Marziani et al. (2009), which involves producing high S/N composite spectra in the 4DE1 context. This was previously performed for our low- z control sample (Bachev et al. 2004), where composites for the five most populated bins were generated. The size of the GTC sample allows only a simple binning into population A and B sources. Composite spectra are shown in Fig. 7 with SPECFIT results in Fig. 8. The GTC binning was partially validated in an earlier section where $\text{CIV}\lambda 1549$ measurements for population A and B sources at high and low z were compared and found to be very similar. Population A–B differences previously established for the low- z sample were also confirmed in the GTC sample. Our best chance for making a reliable comparison of M_{BH} and L/L_{Edd} lies in comparing the high- and low- z composites where the range of source luminosities

Table 7. M_{BH} and L/L_{Edd} estimates from composite spectra.

Spectrum	$\log \lambda L_{\lambda}^a$ [erg s^{-1}]	$\log L$ [erg s^{-1}]	$\log M_{\text{BH}}$ [M_{\odot}]	$\log L/L_{\text{Edd}}$
Pop. A median	45.49	45.99	8.37	−0.56
Pop. B median	45.30	45.80	8.64	−1.02
Pop. A B04 composite	45.03	46.03	8.19	−0.35
Pop. B B04 composite	45.46	46.47	8.86	−0.62

Notes. ^(a) V luminosity for the B04 composites and $1450 \text{ \AA} \lambda L_{\lambda}$ for the GTC medians.

of both samples is small and similar. Using composites yields spectra with a high enough S/N to resolve the 1900 blend and measure FWHM $\text{AlIII}\lambda 1860$ and $\text{SiIII}\lambda 1892$ with reasonable accuracy. We avoided using the other lines as virial estimators.

With the help of a virial broadening estimator, we computed M_{BH} from the standard relation of Vestergaard & Peterson (2006, see Marziani & Sulentic 2012 for a recent review on M_{BH} derivation in quasars). This scaling law is preferred over a more recent formulation (Shen & Liu 2012) because the latter applies most directly to sources with higher luminosity than those in our samples. Table 7 presents estimates of M_{BH} and L/L_{Edd} derived using the virial FWHM measurements listed in Table 5. Values are given for the four median composite spectra displayed in Fig. 7. Median source luminosities are also presented in Table 7. Table 5 also lists FWHM $\text{CIV}\lambda 1549$ values for comparison, which makes it clear that using $\text{CIV}\lambda 1549$ as a virial estimator would yield M_{BH} estimates much higher than those derived from the FWHM of $\text{AlIII}\lambda 1860$ and the FWHM of $\text{SiIII}\lambda 1892$. It is difficult to fully estimate the effects of sample bias in the composite spectra. If the GTC sample is close to random, we reasonably expect most sources to occupy 4DE1 bins A1, A2 and B1. The RL fraction ($n = 2$ usually population B) $\approx 10\%$ is the random expectation. We also identify two candidate extreme population A sources (possible bin A3). All of these observations coupled with the similarity of the population A and B median $\text{CIV}\lambda 1549$ measurements, as well as the population A and B median differences, suggest that our samples are reasonably well matched. Bolometric corrections were applied following Elvis et al. (1994) to compute L/L_{Edd} . We confirm the trend found in low- z samples where the M_{BH} is smaller in population A (than in population B) sources by 0.67 dex and 0.27 dex for low- z and GTC samples. Median L/L_{Edd} values for population A are 0.33 and 0.46 dex higher than those of population B at low and high z .

4. Discussion

There are likely significant numbers of quasars at $z = 2.3$ with luminosities ($L_{\text{bol}} \sim 10^{46} \text{ erg s}^{-1}$) similar to the most luminous local quasars, and SDSS-III/BOSS has recently greatly increased their numbers. It is assumed that such quasars are increasingly numerous at all redshifts higher than $z \approx 0.6$ (Glikman et al. 2011; Ikeda et al. 2012). The GTC sample shows that their spectra are similar to low- z analogs. Our previously defined 4DE1 formalism (Sulentic et al. 2000b, 2007) identified two quasar populations based on optical, UV, and X-ray measurements. We made a first attempt at identifying population A and B sources in the GTC sample using previously established criteria, including presence or absence of a $\text{CIV}\lambda 1549$ blueshift or asymmetry, EW CIV (low for population A and high for population B), low

or high FWHM CIV λ 1549, and line ratios in the 1900 Å blend (Bachev et al. 2004; Sulentic et al. 2007). On this basis, high and low accretors (\propto Eddington ratio) were tentatively identified. The Eddington ratio appears to be the principal driver of 4DE1 differences (e.g., Marziani et al. 2001; Boroson 2002; Yip et al. 2004; Kuraszkiwicz et al. 2009). We find 11 population A and 9 population B sources (omitting the lower z and the red quasar), essentially the same fractional division as observed locally. So far, the low- L quasar population at $z \approx 2.5$ appears to be similar to the low- z one. The population A–B distinction and spectral differences are preserved. Observational and physical parameters of GTC and the control sample (FOS-CS) are found to be consistent.

4.1. A population of moderately accreting quasars at high redshift: are there real evolutionary effects?

The optical luminosity function for quasars (QLF) based on 2dF or 2QZ is well fit by a pure luminosity evolution model at redshifts lower than the redshift of the peak in the quasar population (e.g., Boyle et al. 2000). At $z \approx 0$ and 2.5 we find a turnover absolute magnitude $M_b^* = -22$ and -26 respectively. Thus our samples in the range -23 to -25 are very luminous at low z and underluminous at $z \approx 2.5$. Sources in this luminosity range are still undersampled at $z > 2$, but the first iteration of the BOSS survey (SDSS III: e.g., Palanque-Delabrouille et al. 2013) designed to overcome this deficit, requires a double power-law fit to the QLF with pure luminosity evolution up to $z \approx 1-2$ and a breakdown at higher z (e.g., Richards et al. 2006). At $z \approx 2-2.5$ the onset of the monster quasar population, absent locally, is well developed. The similarity of the $z \approx 2.1-2.3$ sample to the local analogs in the control sample supports the interpretation that we are not sampling the monsters, but rather the underlying quasar population, which grows much more slowly.

Simple expectations for an evolving universe involve an M_{BH} decrease and an L/L_{Edd} increase at higher z (e.g., Kollmeier et al. 2006). A systematic decrease in Eddington ratio after $z \approx 2$ is believed to cause the fading of the quasar population (Cavaliere & Vittorini 2000). However, this effect is dominated by the evolution of the most luminous monster quasars. If we restrict our attention to the less luminous but more numerous population below the OLF turnover luminosity, it is at least conceivable that M_{BH} might be systematically smaller (and the Eddington ratio higher) at an age of ≈ 3 Gyr after the Big Bang than in the local Universe.

The luminosity function can be written as

$$\Phi(L, z)dL = \left[\int \Psi(M_{\text{BH}}, z) P\left(\frac{L}{M_{\text{BH}}}|M_{\text{BH}}, z\right) dM_{\text{BH}} \right] dL, \quad (1)$$

where $\Psi(M_{\text{BH}}, z)$ is the mass function and P the probability of having a given Eddington ratio at mass M_{BH} at z . GTC and FOS-CS have statistically indistinguishable luminosity distribution; however, this does not rule out the possibility of systematic differences: for example, systematically lower masses and higher L/L_{Edd} at high z .

Our best chance for making a reliable comparison of M_{BH} and L/L_{Edd} lies in comparing the high- and low- z composites where the range of source luminosities is narrow and similar for the two samples. Using composites makes it possible to resolve the 1900 blend and measure FWHM AlIII λ 1860 and SiIII λ 1892 with higher accuracy. We assigned a luminosity for the FOS-CS composite from the weighted average of the luminosity of each spectral type used to build the composite itself. We found

that M_{BH} derived from median composites at low and high z are consistent.

We also built a distribution using the FWHM H β (at low z , for the FOS-CS) and the virial FWHM of the GTC sample. Black-hole-mass values computed following the photoionization method of Negrete et al. (2013a) are consistent with scaling-laws values, with the average difference $\delta \log M_{\text{BH}} \approx 0.02 \pm 0.21$. We infer consistent ranges in M_{BH} ($8 \lesssim \log M_{\text{BH}} \lesssim 9$) and L/L_{Edd} at high and low z if the absolute statistical uncertainty of the single-epoch mass estimates (± 0.66 dex) is taken into account. The L/L_{Edd} systematic difference between populations A and B is confirmed at low and high z by both the distribution of L/L_{Edd} and by the L/L_{Edd} values estimated from the composite spectra (Table 7). Differences between composite and sample medians are believed to be mainly due to the different assumptions employed to compute M_{BH} and L/L_{Edd} at low and high z .

Our small sample provides no evidence for large difference in $\Psi(M_{\text{BH}}, z)$ and $P(\frac{L}{M_{\text{BH}}}, z)$. The GTC data allowed us to verify for the first time a population of moderately accreting quasars with masses and Eddington ratios similar to those seen in the local Universe. This does not rule out a systematic evolution in the average Eddington ratio with redshift because the massive M_{BH} that were shining at high z have now disappeared and the GTC sample luminosity places them in the high-luminosity tail of the local quasar luminosity function (Grazian et al. 2000; Croom et al. 2004). The situation depicted for the quasars at $z \approx 2.3$ indeed appears to be highly analogous with those in the local Universe, where most active black holes have masses in the range 10^8-10^9 solar masses, while less massive black holes $10^6-10^7 M_{\odot}$ can be accreting at a higher pace (i.e., they are the local extreme population A sources). In other words, the observation of a similar spread in L/L_{Edd} in the GTC and low- z samples is, within the limit of the present data, consistent with an antihierarchical black hole growth scenario (Hasinger et al. 2005; Brandt & Alexander 2010): black holes in the mass range $10^8-10^9 M_{\odot}$ are expected to have already acquired a large portion of their mass at $z \approx 2.4$ and to be entering a phase of slower growth (e.g., Marconi et al. 2006). Sources with smaller mass and higher Eddington ratio may become more frequent earlier (Kollmeier et al. 2006; Netzer et al. 2007; Trakhtenbrot et al. 2011), or may simply have been undetected in optical surveys (or even in the soft X-ray domain) at $z \approx 2.4$. This latter case should be seriously taken into account since the one object that is heavily obscured, FIRST/F2M J153150.4+242317, shows properties that are most likely of extreme population A (see discussion in Appendix A). Clearly, a larger and less biased sample is needed to gain more constraints on the quasar demographics at $z \approx 2.4$.

4.2. Do population B sources also show CIV λ 1549 blueshifts?

We used estimates of the CIV λ 1549 centroid shift and asymmetry in our separation of high- z population A and B sources. Previous work on a low-redshifts sample found a preponderance of blueshifts in population A sources. The individual shift values listed in Table 4 and the composite profile values in Table 5 fully confirm this population A–B difference. We find a few less consistent values in Table 4, which can be explained in several ways: 1) sources misclassified as population A or B; 2) sources with lower S/N spectra where the shift measurement is less certain; or 3) sources with a somewhat unusual ratio of the BLUE and BC components. The CIV λ 1549 line profile in population A sources is composed of at least two

components: 1) BLUE- usually attributed to a wind or outflow; and 2) BC- a relatively symmetric and unshifted component assumed to be analogous to the primary component seen in $H\beta$ (i.e., the classical BLR used as virial M_{BH} estimator). This is the reason why population B sources lacking the BLUE component show FWHM $\text{CIV}\lambda 1549$ values that agree better with FWHM $H\beta$. Population A sources without a significant blueshift may involve sources where $\text{CIV}\lambda 1549$ is dominated by emission from the unshifted classical BLR component. The overall consistency of the GTC measurements with low- z results is impressive.

The analysis of $\text{CIV}\lambda 1549$ profiles in large SDSS samples of quasars (Richards et al. 2011) suggests that $\text{CIV}\lambda 1549$ blueshifts are quasi-ubiquitous among the RQ majority of quasars. We do not find this at low redshift, where only population A sources show a blueshift. In this paper we also find an absence of population B blueshifts in the higher redshift GTC sample. The population A–B difference motivated us to include $c(\frac{1}{2})$ as the principal 4DE1 diagnostic, which involves high-ionization broad lines (Sulentic et al. 2000a). Clearly, the population B result for the GTC sample is consistent with zero blueshift. Taken at face value, the low-redshift results, and now the GTC sample, suggest that about half the quasars show no $\text{CIV}\lambda 1549$ blueshift. Are our results really in conflict with Richards et al. (2011)? Figure 5 of that paper shows the distribution of $\text{CIV}\lambda 1549$ shift vs. $\log L_{\nu}(1550 \text{ \AA})$ for a large SDSS sample. Of course, the S/N of the vast majority of these spectra are inferior to the worst of our data. The centroid of the distribution reported by Richards et al. (2011) lies near $\log L_{\nu} = 30.8 \text{ erg s}^{-1} \text{ Hz}^{-1}$ and $c(\frac{1}{2})(\text{CIV}\lambda 1549) = -800 \text{ km s}^{-1}$ for RQ quasars. The $\text{CIV}\lambda 1549$ blueshift decreases rapidly for lower luminosity quasars, and our samples concentrate near $\log L_{\nu} \approx 30 \text{ erg s}^{-1} \text{ Hz}^{-1}$ where sources are rare in the SDSS database, as we noted above. The rare equivalent-luminosity SDSS quasars in Fig. 5 of Richards et al. (2011) show $\text{CIV}\lambda 1549$ shifts between -200 (red) and $+1000$ (blue) km s^{-1} . There is a general consistency, allowing for the large uncertainties for most of these shift measurements and also considering that Richards et al. (2011) did not distinguish between population A and B sources. They did distinguish between radio-quiet (RQ) and radio-loud (RL) sources, however. RL sources are mainly population B sources in the 4DE1 context, and RL sources show a $\text{CIV}\lambda 1549$ centroid blueshift in their Fig. 5 (in the L range of our study) of only about 150 km s^{-1} . If RL can be used as a population B surrogate, our results are again roughly consistent with the SDSS as explored in Richards et al. (2011). The blueshift results for luminous quasars do not extend to the lower luminosity quasars studied here, which might be an indication that higher luminosity objects are more likely to have a strong wind component.

4.3. Is there a $\text{CIV}\lambda 1549$ evolutionary Baldwin effect?

Since the 1970s there has been interest in the possibility that $\text{CIV}\lambda 1549$ measurements might provide a way to use quasars as standard candles for cosmology (cf. Bian et al. 2012). Interest was sparked by the discovery of an apparently strong anticorrelation between EW $\text{CIV}\lambda 1549$ and source luminosity in a sample of RL quasars (Baldwin 1977). EW CIV showed a change from $\log W(\text{CIV}\lambda 1549) \approx 2.1$ at $\log L_{\nu}(1450) \approx 30.0 \text{ erg s}^{-1} \text{ Hz}^{-1}$ to $\log W(\text{CIV}\lambda 1549) \approx 0.9$ at $\log L_{\nu}(1450) \approx 31.9 \text{ erg s}^{-1} \text{ Hz}^{-1}$ (presented with appropriate caution). The history of follow-up studies for this Baldwin effect (Sulentic et al. 2000a) revealed an anticorrelation between measurements of correlation strength and sample size (decreasing correlation strength with increasing

sample size). More recently, Eigenvector studies have found that the anticorrelation is most likely intrinsic since quasars at a fixed redshift also show it (Bachev et al. 2004; Baskin & Laor 2004; Marziani et al. 2008). Figure 6 (top panels) shows the distributions of $W(\text{CIV}\lambda 1549)$ for our high- and low-redshift samples. There is no statistically significant difference according to a K-S test. We see the population A–B differences mentioned earlier, but no difference in the EW CIV range between the high- and low- z samples. We find no evidence for a z -dependent $W(\text{CIV}\lambda 1549)$ decrease in the GTC sample.

When the GTC measurements are compared with the data of Kinney et al. (1990), the GTC values are found to be similar to typical values for low- z quasars with the same luminosity, arguing against an evolutionary Baldwin effect. Overlaying the GTC equivalent width values onto the more recent data of Bian et al. (2012) shows that our sample is consistent with the weak anticorrelation detected in large samples. Small samples such as the GTC are prone to statistical fluctuation, however. Considering that the Baldwin effect is a rather weak correlation, there is no point in claiming a detection (or a nondetection) of a Baldwin effect unless the sample exceeds ~ 100 quasars (Sulentic et al. 2000a). We can just comment that we find the full range of observed $W(\text{CIV}\lambda 1549)$ values even in samples with a restricted luminosity and redshift range: as mentioned, the equivalent width dispersion is here not due to a luminosity correlation since we studied a sample with an essentially fixed luminosity. If $W(\text{CIV}\lambda 1549)$ correlates with luminosity-related parameters, it is most likely the source Eddington ratio, that is, the real effect might be what has been called the intrinsic Baldwin effect (e.g., Marziani et al. 2008, 2006).

4.4. Possible interpretation of lower chemical abundance at high z

Several lines of evidence suggest lower chemical abundances in the line-emitting gas of the GTC sample than in the control sample. This effect – first seen in our sample – was probably never detected before because of the strong correlation between z and L in flux-limited samples. It seems unlikely that the strength of intercombination lines with low critical density could be considered a manifestation of the “disappearance” of the NLR observed in some high-luminosity sources (Netzer et al. 2004), since the GTC sample is of ordinary luminosity.

Previous work pointed toward a correlation between Z and redshift, luminosity, M_{BH} , and Eddington ratio. A trend involving increasing Z with redshift pointed out in the early mid-1990s has been disproved as associated with Malmquist bias. At present, the better-defined correlation of the metal content appears to be with luminosity (Shin et al. 2013). This correlation is especially strong, and is confirmed by diagnostics based on narrow lines (Nagao et al. 2006a, 2010). Dietrich et al. (2009) found that the gas metallicity of the broad-line region is supersolar with $3 Z/Z_{\odot}$ in luminous, intermediate-redshift quasars, from measurements of the $\text{NIII}]\lambda 1750/\text{OIII}]\lambda 1663$ and $\text{NV}\lambda 1240/\text{CIV}\lambda 1549$ emission line ratios. Shin et al. (2013) also showed a well-defined correlation between Z and luminosity for PG quasars at low z . A Z – M_{BH} correlation has also been claimed (Matsuoka et al. 2011), in analogy with what was found in galaxies (Matteucci 2012). Last, the possibility of a connection between Z and Eddington ratio has been explored as well. Although a connection between Z and L/L_{Edd} is found in the 4DE1 context, as discussed below, the physical origin of this correlation remains unclear, also because the data shown by

Shin et al. (2013) are still insufficient to prove a statistically unbiased correlation.

We must preliminarily point out that great care should be exerted in analyzing data based on the NV λ 1240/CIV λ 1549 and NV λ 1240/HeII λ 1640 ratios because (1) the intensity of the NV λ 1240 line is very difficult to estimate unambiguously unless a reliable model of the Ly α wings is built, as was done by Shin et al. (2013) and in the present paper; (2) the HeII λ 1640 profile is often shelf-like, the HeII λ 1640 lines is blended with much stronger CIV λ 1549 and is therefore difficult to measure accurately, especially in low S/N conditions.

The present data suggest a metallicity decrease with z in the same luminosity range². Within the limits of our sample (a weak anticorrelation can be spurious in a small sample: in addition, the lower Z also relies on an even smaller number of sources), lowest metallicity sources have Z values around solar or slightly subsolar, while other sources show a supersolar enrichment consistent with the quasar population at the same luminosity. There is a simple interpretation for this finding. The GTC quasars are accreting gas that reflects the chemical composition of the host galaxy; it is known that there is a clear metallicity decrease with z : for fixed host mass $10^{11} M_{\odot}$, the O/H ratio would decrease from 2.5 solar to 1.5 solar, with a steep decrease with lower host masses (Savaglio et al. 2005). For the typical M_{BH} of our sample, the M_{BH} – bulge mass expected at $z \approx 2.35$ (Merloni et al. 2010; Schulze & Wisotzki 2014) involves stellar masses $\log M_{\star} \sim 11 [M_{\odot}]$. In this case we may well expect a metallicity around solar.

The important point here is that we do not have evidence of accretion of “pristine” gas: the metallicity is not highly subsolar. At the same time, the enrichment is, at least in several cases, not as strong as that of many luminous quasars: the accreting gas diagnostic ratios are not demanding any enrichment associated with circumnuclear star formation (Sani et al. 2010; Negrete et al. 2012), and may be well ascribed to gas whose metal enrichment has followed the typical processes of the host galaxy of the interstellar medium. In other words, the black hole is being fed by gas whose composition appears to be normal or close to normal for host galaxies at their cosmic age.

Do these finding allow us to make some more general consideration on the correlations between Z and physical parameters? In the 4DE1 context, there is probably no relation between M_{BH} and Z : the most massive sources in the local Universe, those of population B, do not show evidence of a particular enrichment: the metal-content-sensitive lines (FeII, AlIII λ 1860, NV λ 1240) are all the weakest along the 4DE1 sequence. At the other end of the sequence are the highest accretors: they show strong FeII emission and AlIII λ 1860/SiIII λ 1892 ≥ 0.5 and SiIII λ 1892 \geq CIII λ 1909 in the UV (Marziani & Sulentic 2014a), and evidence of a strong increase in Z , possibly demanding circumnuclear star formation with a top-loaded IMF and/or a special timing in the active nucleus evolution (Negrete et al. 2012). Therefore, a metallicity trend with L/L_{Edd} might be expected. Significant metal enrichment is consistent with a scenario in which the rapidly accreting phase of the quasar black hole follows gas accumulation, collapse, and star formation in the circumnuclear regions (see e.g., Hopkins et al. 2006; Sanders et al. 2009; Teng & Veilleux 2010; Trakhtenbrot et al. 2011). The quasars of the GTC sample do not belong to extreme sources. Their most frequent spectral type is most likely A1 or B1, with at

most two sources whose properties are more consistent with A2 or A3. The Eddington ratio values are modest, and mass-inflow rates are estimated to be in the range $0.3\text{--}1 M_{\odot} \text{ yr}^{-1}$. Therefore, the GTC quasars show properties that are consistent with the $Z - L/L_{\text{Edd}}$ relation suggested by the 4DE1 contextualization.

5. Conclusion

We have analyzed GTC spectra for 22 sources near redshift $z \approx 2.35$ using techniques similar to those employed for low- z quasars observed in the UV by HST-FOS. The latter provide an effective comparison sample of luminosity analogs. The properties of the GTC sample are quite similar to the low-redshift quasars in the sense that we observe roughly equal numbers of population A and B high or low accretors. The same population A–B median properties (and population A–B differences) are seen at high and low redshift – this comparison relies on the strong CIV λ 1549 line that was previously selected as a 4DE1 diagnostic. We find no evidence for an evolutionary Baldwin effect involving CIV λ 1549. We find evidence that the CIV λ 1549 blueshift, apparently quasi-ubiquitous among high-luminosity quasars, is present in only half of both high- and low-redshift quasars in the moderate-luminosity range studied here. It is a high-accreting population A property. If population A sources are on average younger by virtue of their smaller inferred M_{BH} (and higher L/L_{Edd} values), our high-redshift sample does not show any significant increase in the fraction of younger population A sources. However, there is a luminosity selection operating here that lets us miss low M_{BH} sources with M_{BH} significantly below $10^8 M_{\odot}$ even if they are radiating at the Eddington limit (with our magnitude limits no source below $\log M_{\text{BH}} \approx 7.5$ should be detectable even with $L/L_{\text{Edd}} \approx 1$).

Evidence for an excess of lower metallicity quasars in the high-redshift sample was provided by two diagnostic ratios based on strong emission lines as well as by the overall strength of fainter metal lines in population A sources. These finding are consistent with the evolution of metal content in the stellar populations and presumably in the interstellar medium of the host galaxy.

Acknowledgements. Part of this work was supported by Junta de Andalucía through Grant TIC-114 and Proyecto de Excelencia P08-FQM-4205 as well as by the Spanish Ministry for Science and Innovation through Grant AYA2010-15169. P.M. wishes to thank the IAA for supporting her visit in March 2014. D.D. acknowledges support from grant PAPIIT107313, UNAM. Based on observations made with the Gran Telescopio Canarias (GTC), instaled in the Spanish Observatorio del Roque de los Muchachos of the Instituto de Astrofísica de Canarias, in the island of La Palma. We thank all the GTC Staff, and especially René Rutten and Antonio Cabrera, for their support with the observations. We would like to thank Josefa Masegosa for all the fruitful discussions on the subject. We also thank the referee for many useful comments that helped to significantly improve the presentation of the GTC survey. This research has made use of the VizieR catalogue access tool, CDS, Strasbourg, France. The original description of the VizieR service was published in A&AS 143, 23. This research has also made use of the NASA/IPAC Extragalactic Database (NED), which is operated by the Jet Propulsion Laboratory, California Institute of Technology, under contract with the National Aeronautics and Space Administration.

References

- Ahn, C. P., Alexandroff, R., Allende Prieto, C., et al. 2014, ApJS, 211, 17
- Bachev, R., Marziani, P., Sulentic, J. W., et al. 2004, ApJ, 617, 171
- Baskin, A., & Laor, A. 2004, MNRAS, 350, L31
- Bian, W.-H., Fang, L.-L., Huang, K.-L., & Wang, J.-M. 2012, MNRAS, 427, 2881
- Boroson, T. A. 2002, ApJ, 565, 78
- Boroson, T. A. 2011, ApJ, 735, L14
- Boyle, B. J., Jones, L. R., & Shanks, T. 1991, MNRAS, 251, 482
- Boyle, B. J., Shanks, T., Croom, S. M., et al. 2000, MNRAS, 317, 1014

² Note that this effect is not detectable in the Z -sensitive ratios of Table 5 since the median combination of spectra tends to cancel a trend that is seen in a minority of sources.

- Brandt, W. N., & Alexander, D. M. 2010, Proc. of the National Academy of Science, 107, 7184
- Brandt, W. N., Alexander, D. M., Hornschemeier, A. E., et al. 2001, AJ, 122, 2810
- Brightman, M., Silverman, J. D., Mainieri, V., et al. 2013, MNRAS, 433, 2845
- Brotherton, M. S., Tran, H. D., Becker, R. H., et al. 2001, ApJ, 546, 775
- Brühweiler, F., & Verner, E. 2008, ApJ, 675, 83
- Cavaliere, A., & Vittorini, V. 2000, ApJ, 543, 599
- Cheng, F.-Z., Danese, L., Franceschini, A., & de Zotti, G. 1985, MNRAS, 212, 857
- Collin, S., Kawaguchi, T., Peterson, B. M., & Vestergaard, M. 2006, A&A, 456, 75
- Crampton, D., Schade, D., & Cowley, A. P. 1985, AJ, 90, 987
- Crampton, D., Janson, T., Durrell, P., Cowley, A. P., & Schmidtke, P. C. 1988, AJ, 96, 816
- Croom, S. M., Smith, R. J., Boyle, B. J., et al. 2001, MNRAS, 322, L29
- Croom, S. M., Smith, R. J., Boyle, B. J., et al. 2004, MNRAS, 349, 1397
- Dietrich, M., Mathur, S., Grupe, D., & Komossa, S. 2009, ApJ, 696, 1998
- Dong, X.-B., Wang, T.-G., Wang, J.-G., et al. 2009, ApJ, 703, L1
- Dultzin, D., Martínez, M. L., Marziani, P., Sulentic, J. W., & Negrete, A. 2011, in Proc. of the conference Narrow-Line Seyfert 1 Galaxies and their place in the Universe, April 4–6, Milano, Italy, eds. L. Foschini, L. Colpi, L. Gallo, et al. (Proc. of Science: Trieste)
- Elvis, M., Wilkes, B. J., McDowell, J. C., et al. 1994, ApJS, 95, 1
- Eracleous, M., & Halpern, J. P. 2003, ApJ, 599, 886
- Fan, X. 2006, New Astron. Rev., 50, 665
- Ferland, G. J., Baldwin, J. A., Korista, K. T., et al. 1996, ApJ, 461, 683
- Ferland, G. J., Porter, R. L., van Hoof, P. A. M., et al. 2013, Rev. Mex. Astron. Astrofis., 49, 137
- Glikman, E., Helfand, D. J., White, R. L., et al. 2007, ApJ, 667, 673
- Glikman, E., Djorgovski, S. G., Stern, D., et al. 2011, ApJ, 728, L26
- Glikman, E., Urrutia, T., Lacy, M., et al. 2012, ApJ, 757, 51
- Gordon, K. D., & Clayton, G. C. 1998, ApJ, 500, 816
- Gordon, K. D., Clayton, G. C., Misselt, K. A., Landolt, A. U., & Wolff, M. J. 2003, ApJ, 594, 279
- Grazian, A., Cristiani, S., D'Odorico, V., Omizzolo, A., & Pizzella, A. 2000, AJ, 119, 2540
- Griffith, M. R., Wright, A. E., Burke, B. F., & Ekers, R. D. 1994, ApJS, 90, 179
- Hamann, F., & Ferland, G. 1993, ApJ, 418, 11
- Hamann, F., Korista, K. T., Ferland, G. J., Warner, C., & Baldwin, J. 2002, ApJ, 564, 592
- Hasinger, G., Miyaji, T., & Schmidt, M. 2005, A&A, 441, 417
- Hopkins, P. F., Hernquist, L., Cox, T. J., et al. 2006, ApJS, 163, 1
- Hu, C., Wang, J.-M., Ho, L. C., et al. 2008, ApJ, 683, L115
- Ikedo, H., Nagao, T., Matsuoka, K., et al. 2012, ApJ, 756, 160
- Juarez, Y., Maiolino, R., Mujica, R., et al. 2009, A&Ap, 494, L25
- Kinney, A. L., Rivolo, A. R., & Koratkar, A. P. 1990, ApJ, 357, 338
- Koehler, T., Groote, D., Reimers, D., & Wisotzki, L. 1997, A&A, 325, 502
- Kollmeier, J. A., Onken, C. A., Kochanek, C. S., et al. 2006, ApJ, 648, 128
- Kriss, G. 1994, Astronomical Data Analysis Software and Systems III, ASP Conf. Ser., 61, 437
- Kuraszkiewicz, J., Wilkes, B. J., Schmidt, G., et al. 2009, ApJ, 692, 1180
- Kurk, J. D., Walter, F., Fan, X., et al. 2007, ApJ, 669, 32
- Marconi, A., Comastri, A., Gilli, R., et al. 2006, Mem. Soc. Astron. It., 77, 742
- Marziani, P., & Sulentic, J. W. 2012, New Astron. Rev., 56, 49
- Marziani, P., & Sulentic, J. W. 2014a, Adv. Space Res., 54, 1331
- Marziani, P., & Sulentic, J. W. 2014b, MNRAS, 442, 1211
- Marziani, P., Sulentic, J. W., Zwitter, T., Dultzin-Hacyan, D., & Calvani, M. 2001, ApJ, 558, 553
- Marziani, P., Sulentic, J. W., Zamanov, R., et al. 2003, ApJS, 145, 199
- Marziani, P., Dultzin-Hacyan, D., & Sulentic, J. W. 2006, Accretion onto Supermassive Black Holes in Quasars: Learning from Optical/UV Observations (New Developments in Black Hole Research), 123
- Marziani, P., Dultzin, D., & Sulentic, J. W. 2008, in Rev. Mex. Astron. Astrofis. Conf. Ser., 32, 103
- Marziani, P., Sulentic, J. W., Stirpe, G. M., Zamfir, S., & Calvani, M. 2009, A&Ap, 495, 83
- Marziani, P., Sulentic, J. W., Negrete, C. A., et al. 2010, MNRAS, 409, 1033
- Marziani, P., Sulentic, J. W., Plauchu-Frayn, I., & del Olmo, A. 2013, ApJ, 764
- Matsuoka, K., Nagao, T., Marconi, A., Maiolino, R., & Taniguchi, Y. 2011, A&A, 527, A100
- Matteucci, F. 2012, Chemical Evolution of Galaxies (Springer Verlag)
- Merloni, A., Bongiorno, A., Bolzonella, M., et al. 2010, ApJ, 708, 137
- Metzroth, K. G., Onken, C. A., & Peterson, B. M. 2006, ApJ, 647, 901
- Nagao, T., Maiolino, R., & Marconi, A. 2006a, A&A, 447, 863
- Nagao, T., Marconi, A., & Maiolino, R. 2006b, A&Ap, 447, 157
- Nagao, T., Maiolino, R., Marconi, A., Matsuoka, K., & Taniguchi, Y. 2010, in IAU Symp. 267, eds. B. M. Peterson, R. S. Somerville, & T. Storchi-Bergmann, 73
- Negrete, A., Dultzin, D., Marziani, P., & Sulentic, J. 2012, ApJ, 757, 62
- Negrete, C. A., Dultzin, D., Marziani, P., & Sulentic, J. W. 2013a, ApJ, 771, 31
- Negrete, C. A., Dultzin, D., Marziani, P., & Sulentic, J. W. 2013b Adv. Space Res., in press, <http://www.sciencedirect.com/science/article/pii/S027311713007400#>
- Negrete, C. A., Dultzin, D., Marziani, P., & Sulentic, J. W. 2014, ApJ, submitted [[arXiv:1404.1673](https://arxiv.org/abs/1404.1673)]
- Netzer, H. 2013, The Physics and Evolution of Active Galactic Nuclei (Cambridge University Press)
- Netzer, H., & Trakhtenbrot, B. 2007, ApJ, 654, 754
- Netzer, H., Shemmer, O., Maiolino, R., et al. 2004, ApJ, 614, 558
- Netzer, H., Lira, P., Trakhtenbrot, B., Shemmer, O., & Cury, I. 2007, ApJ, 671, 1256
- Onken, C. A., & Peterson, B. M. 2002, ApJ, 572, 746
- Osmer, P. S., & Hewett, P. C. 1991, ApJS, 75, 273
- Palanque-Delabrouille, N., Magneville, C., Yèche, C., et al. 2013, A&A, 551, A29
- Papovich, C., Cool, R., Eisenstein, D., et al. 2006, AJ, 132, 231
- Peterson, B. M., & Wandel, A. 1999, ApJ, 521, L95
- Richards, G. T., Croom, S. M., Anderson, S. F., et al. 2005, MNRAS, 360, 839
- Richards, G. T., Lacy, M., Storrie-Lombardi, L. J., et al. 2006, ApJS, 166, 470
- Richards, G. T., Kruczek, N. E., Gallagher, S. C., et al. 2011, AJ, 141, 167
- Runnoe, J. C., Brotherton, M., Shang, Z., Wills, B., & DiPompeo, M. 2013, MNRAS, 429, 135
- Sanders, D. B., Kartaltepe, J. S., Kewley, L. J., et al. 2009, in The Starburst-AGN Connection, eds. W. Wang, Z. Yang, Z. Luo, & Z. Chen, ASP Conf. Ser., 408, 3
- Sani, E., Lutz, D., Risaliti, G., et al. 2010, MNRAS, 403, 1246
- Savaglio, S., Glazebrook, K., Le Borgne, D., et al. 2005, ApJ, 635, 260
- Schmidt, M. 1968, ApJ, 151, 393
- Schmidt, M., & Green, R. F. 1983, ApJ, 269, 352
- Schmidt, M., Schneider, D. P., & Gunn, J. E. 1995, AJ, 110, 68
- Schneider, D. P., Richards, G. T., Hall, P. B., et al. 2010, AJ, 139, 2360
- Schulze, A., & Wisotzki, L. 2014, MNRAS, 438, 3422
- Searle, L. 1971, ApJ, 168, 327
- Shemmer, O., Netzer, H., Maiolino, R., et al. 2004, ApJ, 614, 547
- Shen, Y., & Liu, X. 2012, ApJ, 753, 125
- Shin, J., Woo, J.-H., Nagao, T., & Kim, S. C. 2013, ApJ, 763, 58
- Silverman, J. D., Green, P. J., Barkhouse, W. A., et al. 2005, ApJ, 618, 123
- Sulentic, J. W., Marziani, P., & Dultzin-Hacyan, D. 2000a, ARA&A, 38, 521
- Sulentic, J. W., Zwitter, T., Marziani, P., & Dultzin-Hacyan, D., 2000b, ApJ, 536, L5
- Sulentic, J. W., Marziani, P., Zwitter, T., Dultzin-Hacyan, D., & Calvani, M. 2000c, ApJ, 15, L15
- Sulentic, J. W., Marziani, P., Zamanov, R., et al. 2002, ApJ, 566, L71
- Sulentic, J. W., Zamfir, S., Marziani, P., et al. 2003, ApJ, 597, L17
- Sulentic, J. W., Repetto, P., Stirpe, G. M., et al. 2006, A&Ap, 456, 929
- Sulentic, J. W., Bachev, R., Marziani, P., Negrete, C. A., & Dultzin, D. 2007, ApJ, 666, 757
- Sulentic, J. W., Zamfir, S., Marziani, P., & Dultzin, D. 2008, in Rev. Mex. Astron. Astrofis. Conf. Ser., 32, 51
- Sulentic, J., Marziani, P., & Zamfir, S. 2011, Baltic Astron., 20, 427
- Teng, S. H., & Veilleux, S. 2010, ApJ, 725, 1848
- Trakhtenbrot, B., Netzer, H., Lira, P., & Shemmer, O. 2011, ApJ, 730, 7
- Véron-Cetty, M.-P., & Véron, P. 2010, A&A, 518, A10
- Vestergaard, M., & Peterson, B. M. 2006, ApJ, 641, 689
- Vestergaard, M., & Wilkes, B. J. 2001, ApJS, 134, 1
- Wang, H., Zhou, H., Yuan, W., & Wang, T. 2012, ApJ, 751, L23
- Weedman, D. W. 1985, ApJS, 57, 523
- Willott, C. J., Delorme, P., Reylé, C., et al. 2010, AJ, 139, 906
- Wolf, C., Meisenheimer, K., Röser, H.-J., et al. 1999, A&A, 343, 399
- Yip, C. W., Connolly, A. J., Vanden Berk, D. E., et al. 2004, AJ, 128, 2603
- York, D. G., Khare, P., Vanden Berk, D., et al. 2006, MNRAS, 367, 945
- Zamfir, S., Sulentic, J. W., & Marziani, P. 2008, MNRAS, 387, 856
- Zamfir, S., Sulentic, J. W., Marziani, P., & Dultzin, D. 2010, MNRAS, 403, 1759
- Zhou, H., Wang, T., Yuan, W., Lu, H., Dong, X., Wang, J., & Lu, Y., 2006, ApJS, 166, 128

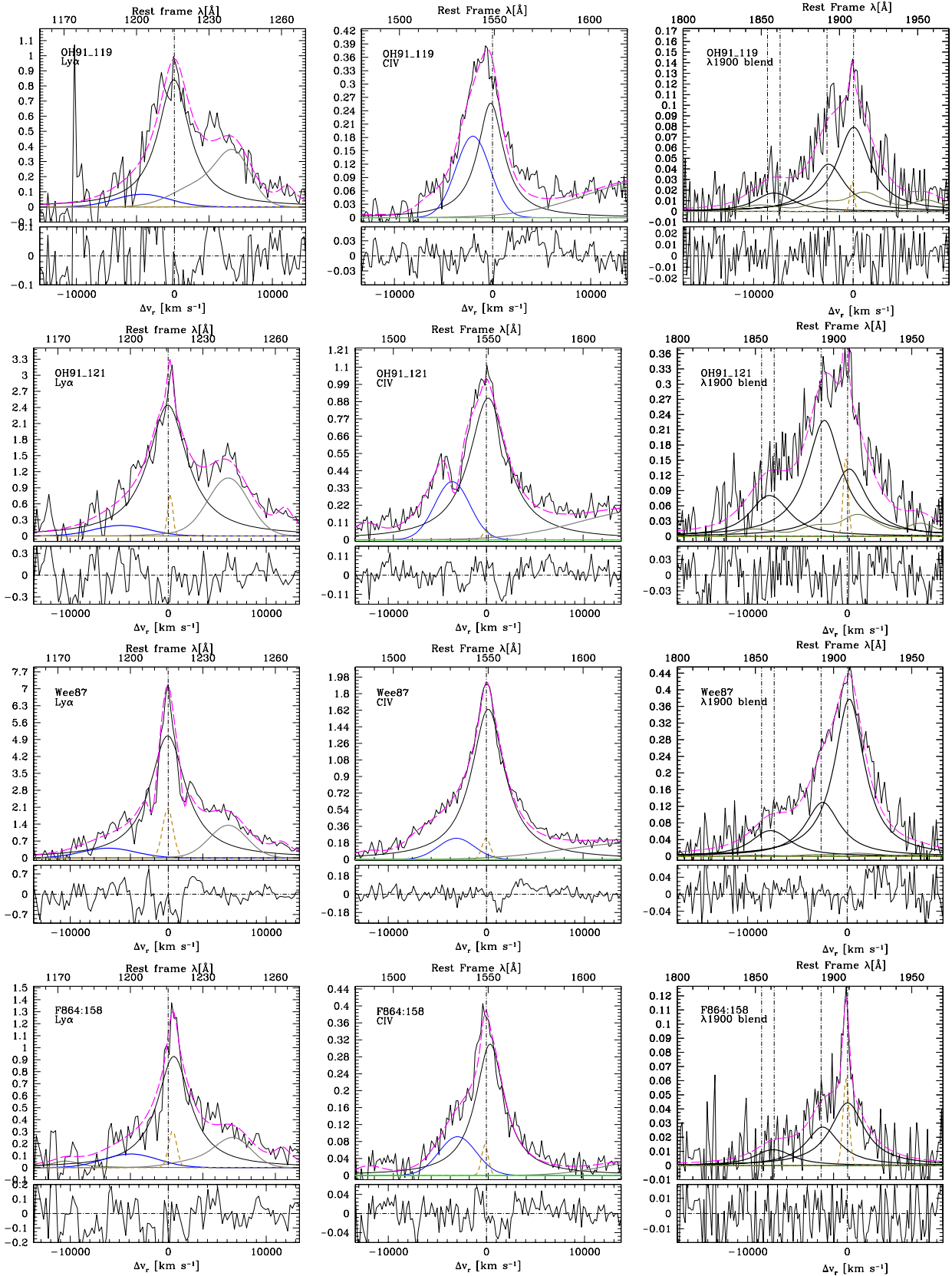


Fig. 4. Results of the line-fit analysis on the Ly α (left panel) CIV λ 1549 (middle) and 1900 Å emission features for population A sources. The lines are shown after continuum subtraction. The magenta dashed line shows the full model of the emission features and intervening narrow absorptions, if present. The thick black lines show the broad components of the prominent emission lines. The thick blue line traces the BLUE component. The NV λ 1240 line on the red side of the Ly α profile is traced by a gray line that includes BC and BLUE. Orange lines are narrow-line components. The lower panel of each frame shows the residuals between the line model and the observations as a function of radial velocity from rest frame (for CIII] λ 1909 in the case of the 1900 blend).

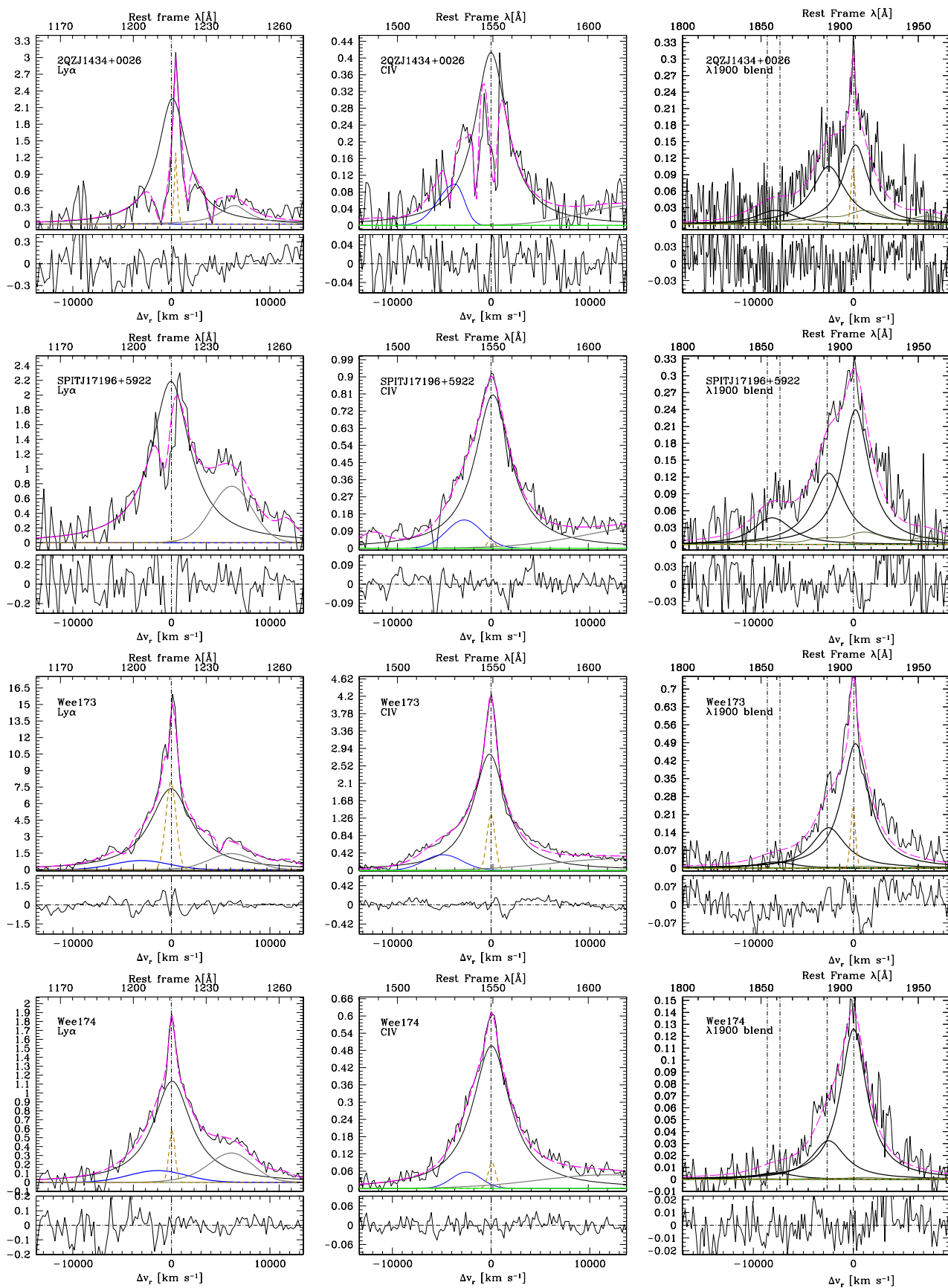


Fig. 4. continued.

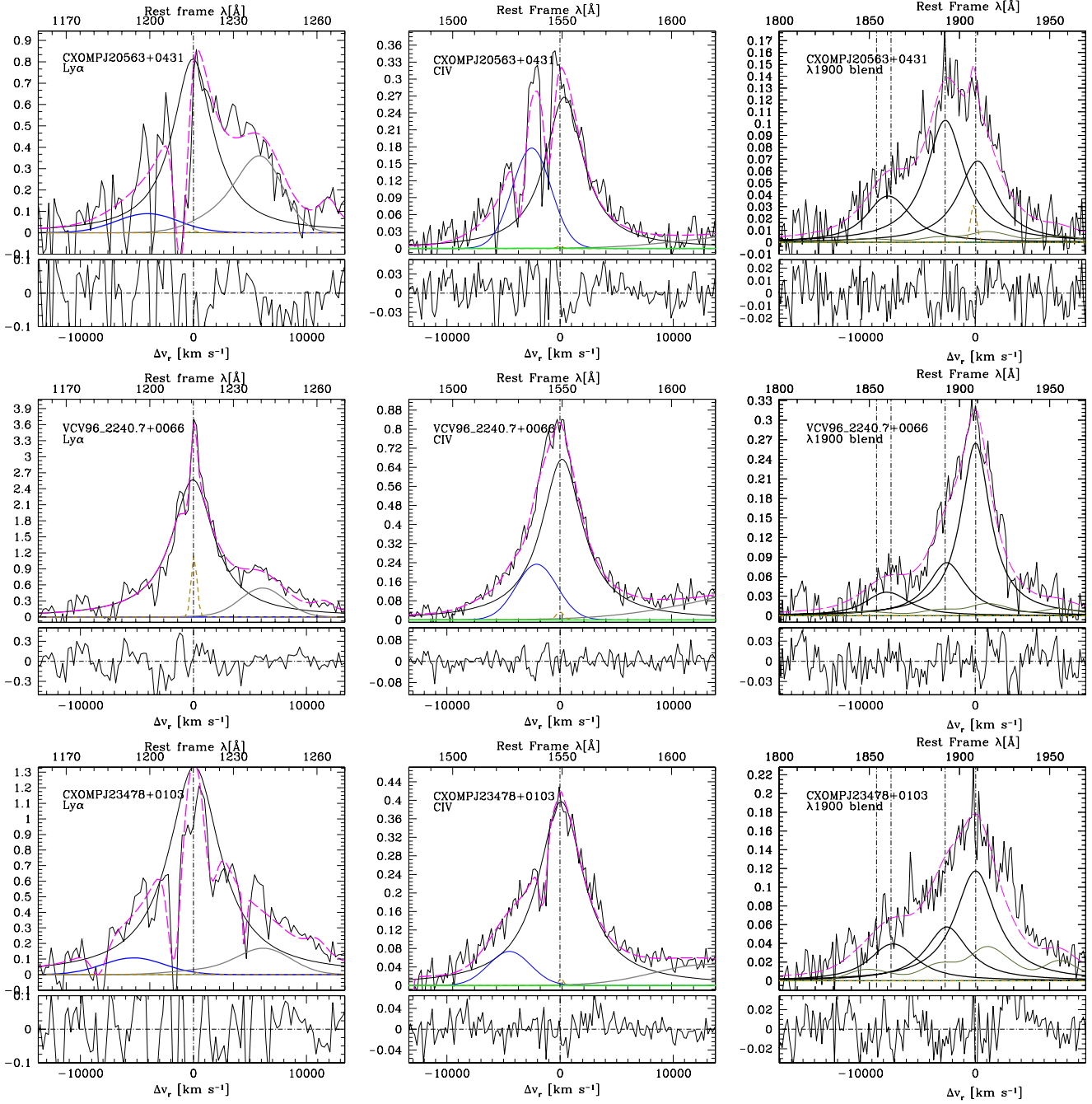


Fig. 4. continued.

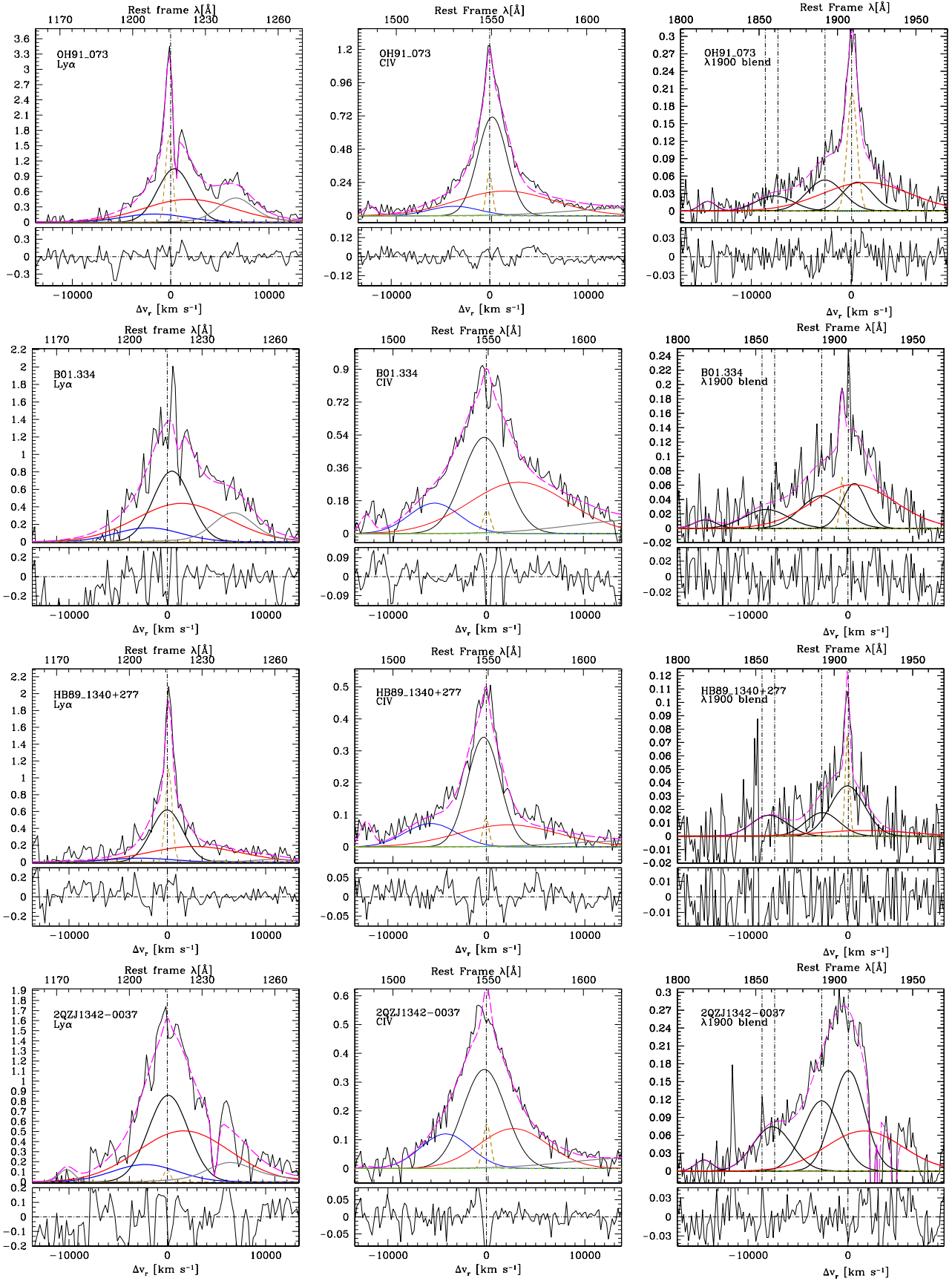


Fig. 5. Results of the line-fit analysis on the Ly α (left panel) CIV λ 1549 (middle) and 1900 Å emission features for population B sources. The meanings of symbols and colors is as in the previous figure. The VBC assumed to be present in the population B emission line profiles is traced by a thick red line.

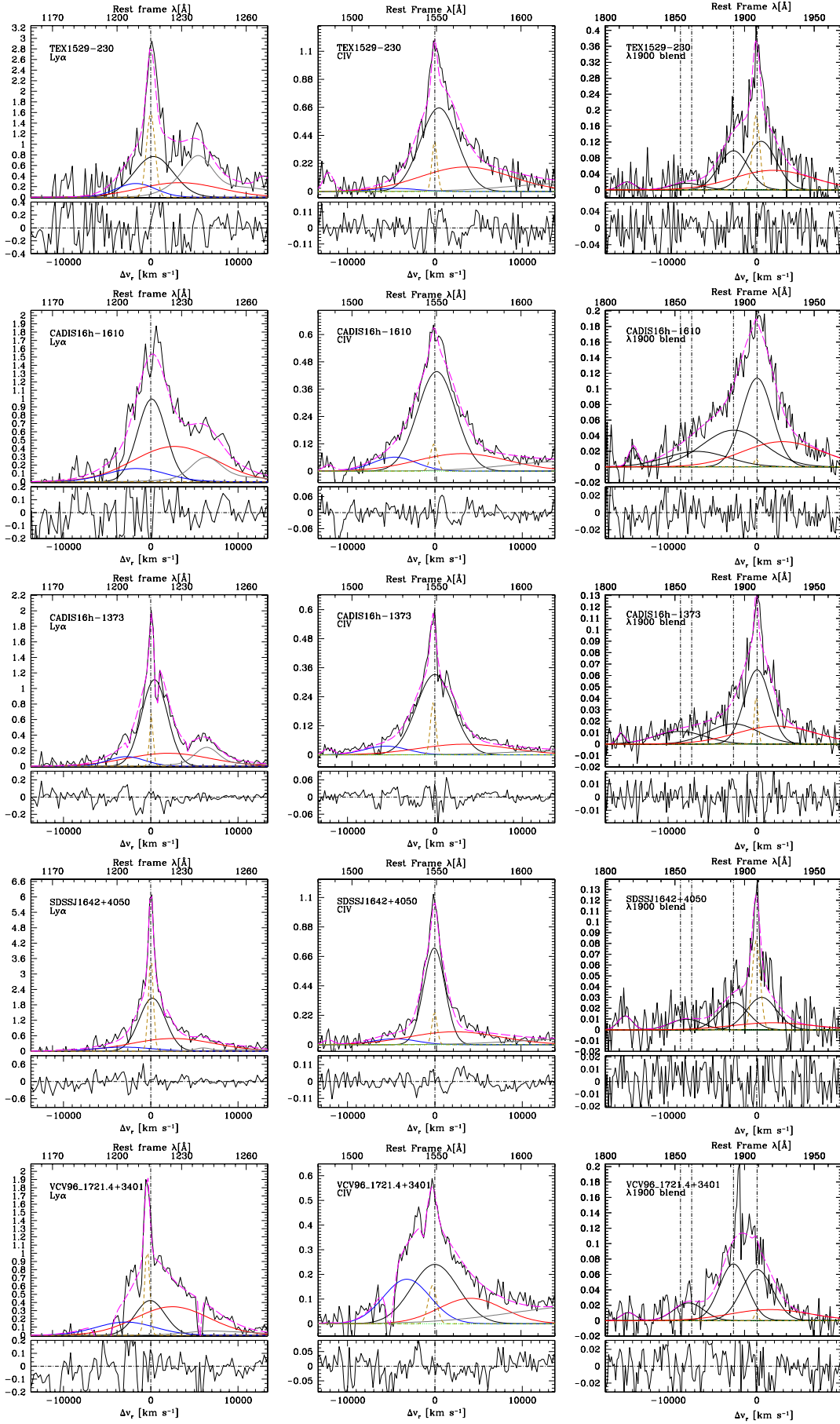


Fig. 5. continued.

Appendix A: Examining a reddened quasar (tip of the iceberg?) observed by GTC

Dust-reddened and obscured quasars play an increasingly important role in the relationship between the growth of supermassive black holes and the evolution of galaxies on cosmic scales. Recently, a new co-evolution scenario has emerged from the identification of a significant sample of red QSOs (e.g., Glikman et al. 2012, and references therein) in which the reddening is not linked to the central disk/torus phenomenon, but is associated with cold dust from the host galaxy that would also be experiencing starburst processes. In this scenario red QSOs constitute a population of young high-accreting quasars that are probably involved with a feedback mechanism. They could be precursors of the blue luminous quasars that are revealed when the dusty cocoon is swept away.

In our random selection of quasars from the Véron-Cetty & Véron (2010) catalog we included one of these red quasars. SDSS J153150.41+242317.7 (also known as FIRST 15318+2423 and F2M1531+2423) was first identified as a red QSO by Glikman et al. (2007) from a sample of FIRST-2MASS candidates. They obtained NIR spectroscopy and detected broad $H\alpha$ and $H\beta$ emission lines with $z \approx 2.287$. Our GTC spectrum is shown in Fig. A.1, where the highly reddened continuum is obvious as well as the presence of $Ly\alpha$, $HeII\lambda 1640$ and deep absorptions at the wavelengths of broad lines such as $CIV\lambda 1549$ and $CIII]\lambda 1909$ from which it can be classified as a mini-BAL. Taking into account all these lines, we obtained a redshift of 2.284.

We have estimated the reddening of this object, parametrized by the color excess $E(B-V)$, by fitting its UV continuum with three quasar templates, excluding the regions of broad emission lines ($Ly\alpha$, $CIV\lambda 1549$, $CIII]\lambda 1909$, Fe band). To redden the templates we used an SMC extinction law (Gordon & Clayton 1998; Gordon et al. 2003), which appears to be the most appropriate reddening law to model dust reddening in quasars (York et al. 2006). We assumed an R_V coefficient of 3.07 for the extinction law. Templates employed included two derived GTC composite spectra corresponding to populations A and B, which provide internal concordance since they were obtained from our quasar sample with the same instrumental setup, and also a third template involving the composite FIRST Bright Quasar Survey spectrum (FBQS; Brotherton et al. 2001).

The three fits yield essentially the same value for the color excess. In the first two cases, using the population A and B composites, we obtained $E(B-V) = 0.41 \pm 0.01$, while the FBQS

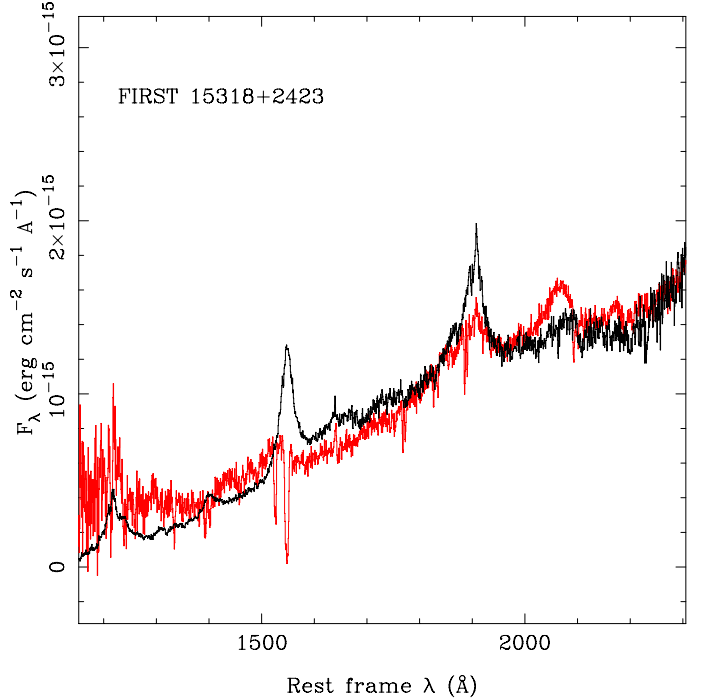


Fig. A.1. Rest-frame spectrum of FIRST J15318+2423 (red). The abscissa is the rest-frame wavelength, the ordinate is the rest-frame specific flux. The reddened population A template is shown in black. See text for more details.

template yields $E(B-V) = 0.40$, all cases with a high correlation coefficient (≥ 0.97). Taking into account the estimated extinction, FIRST15318 becomes the brightest quasar in our sample with $M_B \approx -26.3$. In Fig. A.1 we have plotted the fitted reddened population A template over the observed spectrum. Attempts to learn more about its nature are difficult using the present data. A formal fitting of the red quasar continuum gives a slightly better solution than a reddened population A spectrum, but both population A and B fits yield similar results. By taking advantage of NIR spectroscopic data (Glikman et al. 2007, 2012), we modeled the $H\alpha$ and $H\beta$ lines. The fit for $H\alpha$ involves a Lorentzian profile with an $FWHM$ (BC) $\approx 3400 \text{ km s}^{-1}$ that identifies FIRST15318 as a population A quasar in concordance with the UV continuum we fitted. In the $H\beta$ region, the spectrum is noisier, but clearly shows the strong FeII emission characteristic of highly accreting population A sources (spectral type A2 or A3).